The Astrophysical Journal, 1002:176 (23pp), 2026 May 10 https://doi.org/10.3847/1538-4357/ae5e6a

JWST/MIRI Hydrocarbon and Water Absorption in the Wind of a Young Disk: Signatures of Pebble Drift and Carbon Grain Sublimation

María José Colmenares[1], Edwin A. Bergin[1], Ke Zhang[2], Geoffrey A. Blake[3], Klaus M. Pontoppidan[3,4], Alexa R. Anderson[5], John Carr[6], Emma Dahl[7], Joan Najita[8], Jonathan P. Williams[5], Colette Salyk[9], Till Kaeufer[10], Mayank Narang[4], Ilaria Pascucci[11], Benot Tabone[12], Lucas Cieza[13,14], Miguel Vioque[15], Adrien Houge[16], Sebastiaan Krijt[17], Aditya M. Arabhavi[4], Giovanni Rosotti[18], John Carpenter[19], Feng Long (龙凤)[20], Paola Pinilla[21], Jayatee Kanwar[1], Eshan Raul[2], Karina Mauco[22], James Miley[23], Abygail Waggoner[2], and The JDISCS Collaboration

[1] Department of Astronomy, University of Michigan, 1085 South University Avenue, Ann Arbor, MI 48109, USA; mjcolmen@umich.edu
[2] Department of Astronomy, University of Wisconsin-Madison, 475 N Charter Street, Madison, WI 53706, USA
[3] Division of Geological and Planetary Sciences, California Institute of Technology, MC 150-21, 1200 E California Boulevard, Pasadena, CA 91125, USA
[4] Jet Propulsion Laboratory, California Institute of Technology, 4800 Oak Grove Drive, Pasadena, CA 91109, USA
[5] Institute for Astronomy, University of Hawai'i at Mānoa, 2680 Woodlawn Drive, Honolulu, HI 96822, USA
[6] Department of Astronomy, University of Maryland, College Park, MD 20742, USA
[7] California Institute of Technology, 4800 Oak Grove Drive, Pasadena, CA 91109, USA
[8] NSFs NOIRLab, 950 N. Cherry Avenue, Tucson, AZ 85719, USA
[9] Vassar College, 124 Raymond Avenue, Poughkeepsie, NY 12604, USA
[10] Department of Physics and Astronomy, University of Exeter, Exeter EX4 4QL, UK
[11] Lunar and Planetary Laboratory, University of Arizona, Tucson, AZ 85721, USA
[12] Université Paris-Saclay, CNRS, Institut d'Astrophysique Spatiale, F-91405 Orsay, France
[13] Instituto de Estudios Astrofísicos, Universidad Diego Portales, Av. Ejercito 441, Santiago, Chile
[14] Millennium Nucleus on Young Exoplanets and their Moons (YEMS), Santiago, Chile
[15] European Southern Observatory, Karl-Schwarzschild-Str. 2, 85748, Garching bei München, Germany
[16] Center for Star and Planet Formation, GLOBE Institute, University of Copenhagen, Øster Voldgade 5-7, 1350 Copenhagen, Denmark
[17] School of Physics and Astronomy, University of Exeter, Stocker Road, Exeter, EX4 4QL, UK
[18] Dipartimento di Fisica, Università degli Studidi Milano, Via Celoria 16, I-20133 Milano, Italy
[19] Joint ALMA Observatory, Alonso de Córdova 3107, Vitacura, Santiago 763-0355, Chile
[20] Kavli Institute for Astronomy and Astrophysics, Peking University, Beijing 100871, People's Republic of China
[21] Mullard Space Science Laboratory, University College London, Holmbury St Mary, Dorking, Surrey RH5 6NT, UK
[22] Universidad Nacional Autónoma de México, Instituto de Astronomía, AP 106, Ensenada 22800, BC, Mexico
[23] Departamento de Física, Universidad de Santiago de Chile, Avenida Victor Jara 3659, Santiago, Chile
Received 2026 February 16; revised 2026 March 22; accepted 2026 April 9; published 2026 May 6

Abstract

We present JWST/MIRI-MRS observations of ISO-Oph 37, a highly inclined flat-spectrum ($\lesssim$1 Myr old) source, to investigate the chemical composition and dynamical origin of its inner-disk gas. The spectrum reveals a rich combination of molecular emission and absorption: H_2O, CO, and OH are detected in emission, while strong absorption is observed from CO, H_2O, CO_2, HCN, C_2H_2, and CH_4, with no detectable ice absorption features. Local thermodynamic equilibrium slab modeling of the absorption yields excitation temperatures of $T_{ex} \sim 400$–600 K and column densities of $\log N/\mathrm{cm}^2 \sim 16$–$19$, characteristic of warm gas located within the inner few astronomical unit. The absorption lines are significantly blueshifted relative to the systemic velocity, with mid-IR lines exhibiting larger shifts than near-IR CO absorption. This velocity structure points to a velocity- and temperature-stratified molecular disk wind. In this framework, the absorption directly samples disk material lifted from the inner disk surface, preserving the chemical imprint of the wind-launching region. Along the line of sight, ISO-Oph 37 is unusually hydrocarbon-rich compared to other known absorption systems (GV Tau N and IRS 46), exhibiting high $(C_2H_2+CH_4)$/HCN, $(C_2H_2+CH_4)$/CO, and H_2O/CO column density ratios, while the CO and HCN columns remain broadly typical. We find that these molecular ratios are best explained by enhancement of both hydrocarbons and water, driven by inward drift and sublimation of icy pebbles and by thermal processing of carbonaceous grains at the soot line. ISO-Oph 37 thus demonstrates that carbon-rich inner-disk chemistry can be established early in disk evolution and that it can be directly probed through molecular absorption in disk winds.

Unified Astronomy Thesaurus concepts: Protoplanetary disks (1300); Circumstellar disks (235); Protostars (1302); Planet formation (1241); Astrochemistry (75)

1. Introduction

Understanding the carbon budget in the inner regions of protoplanetary disks is central to piecing together the formation of terrestrial planets and the chemistry from which they emerge (N. Madhusudhan 2012; K. I. Öberg &

E. A. Bergin 2021; E. A. Bergin et al. 2024). Carbon-bearing species ranging from simple volatiles like CO_2 and CH_4 to larger hydrocarbons such as C_2H_2 play pivotal roles in disk chemistry, influencing condensable carbon carriers, and the initial conditions for planetary atmospheres, as well as the bulk carbon content of terrestrial planets. The unprecedented mid-infrared sensitivity and spectral resolution of the James Webb Space Telescope (JWST; J. Rigby et al. 2023) has recently unveiled a rich inventory of hydrocarbons in inner disks, including CH_4, C_2H_2, and even larger carbon chains, underscoring a carbon-rich chemistry with C/O ratios exceeding unity in some systems (B. Tabone et al. 2023; A. M. Arabhavi et al. 2024; M. J. Colmenares et al. 2024; J. Kanwar et al. 2024, 2025). These discoveries highlight the presence of substantial carbon reservoirs in the warm inner disk.

Prior to JWST, much of our understanding of inner-disk chemistry came from Spitzer/Infrared Spectrograph (IRS) surveys, which revealed numerous molecules such as H_2O, HCN, C_2H_2, OH, and CO_2, predominantly in emission from the warm surface layers of disks within a few astronomical units (I. Pascucci et al. 2009; K. M. Pontoppidan et al. 2010; J. S. Carr & J. R. Najita 2011; C. Salyk et al. 2011; I. Pascucci et al. 2013). These observations established that disks are chemically active environments where both oxygen- and carbon-bearing molecules are abundant. An emerging trend has suggested that as a given disk evolves, the inner gas becomes more carbon-rich, in line with transport-chemistry models in which icy pebble drift and trapping beyond the H_2O and CO_2 snowlines sequester oxygen while grain-surface processing and inward gas flows can deliver carbon-bearing volatiles (including CH_4) to the inner disk, raising the gas-phase C/O ratio (J. Mah et al. 2023, 2024; A. D. Sellek & E. F. van Dishoeck 2025). Early JWST-MIRI spectra provide supporting evidence, with some disks at later stages showing enhanced hydrocarbons and elevated C/O (A. M. Arabhavi et al. 2025; H. Jang et al. 2025; F. Long et al. 2025).

However, the chemical makeup of protoplanetary disks has not always revealed itself through molecular emission lines. A small but important subset of Spitzer targets, most notably the nearly edge-on systems IRS 46 and GV Tau, exhibit strong molecular absorption features (F. Lahuis et al. 2006; J. E. Bast et al. 2013). In these sources, C_2H_2, CO_2, and HCN are detected in absorption against the warm continuum of the inner disk, with excitation temperatures of ∼400–700 K for C_2H_2 and HCN and ∼250 K for CO_2. Absorption offers a complementary and often more direct constraint on column densities along the line of sight to the inner continuum, reducing degeneracies tied to emitting area that can affect emission analyses, and thereby helping to localize warm gas vertically and radially in the inner disk (e.g., J. E. Bast et al. 2013). The interpretation of these rare absorption sources has centered on their geometry since they are highly inclined disks that place warm gas in front of the bright continuum (E. L. Gibb & D. Horne 2013), but additional scenarios such as disk winds or accretion inflows have also been invoked (F. Lahuis et al. 2006; G. W. Doppmann et al. 2008; J. R. Najita et al. 2021).

With JWST, absorption is now more easily identified; surveys of protostars and edge-on systems report mid-IR absorption (ices and, in some cases, gas) coexisting with line emission. These observations expand the limited Spitzer sample and reframe absorption as both a geometric and evolutionary diagnostic rather than a rarity (N. G. C. Brunken et al. 2024; M. L. van Gelder et al. 2024a; H. Tyagi et al. 2025; M. K. McClure et al. 2025). In such datasets, H_2 rotational lines and forbidden lines (e.g., [Ne II], [Ne III], [Fe II], [Ar II/III]) can be spatially extended, enabling separation of disk, envelope, and wind/jet contributions relative to the continuum (e.g., N. Arulanantham et al. 2024; N. S. Bajaj et al. 2024; M. Narang et al. 2025, 2026; I. Pascucci et al. 2025).

A persistent difficulty in studying most molecular absorption features is the disentanglement of the disk from its environment. Many systems still retain residual envelopes from the star formation process, or are located in regions of high extinction, such as ρ Ophiuchi. This complicates the determination of their ages and evolutionary states, as envelope emission, scattered light, or foreground absorption can contaminate the disk signatures (M. K. McClure et al. 2010; J. A. Sturm et al. 2024). Moreover, the mid-infrared extinction law in ρ Ophiuchi departs from diffuse interstellar medium (ISM) prescriptions and varies with column density, which can alter continuum slopes and bias spectral energy distribution (SED) classifications, complicating the separation of truly embedded sources from edge-on Class II disks (M. McClure 2009; N. L. Chapman et al. 2009; E. Furlan et al. 2011). As a result, connecting molecular detections to disk age and C/O evolution has remained challenging. The unprecedented spatial and spectral resolution of JWST-MIRI now enables separation of disk and extended components, even in highly inclined and extinguished systems, offering a way to disentangle disk chemistry from environmental effects.

Against this backdrop, we present new JWST-MIRI observations of ISO-Oph 37 (also called LFAM 3 or 2MASS J16262357-2424394), a K7 flat-spectrum young stellar object (YSO) in the ρ Ophiuchi star-forming region. Table 1 lists a compilation of its observed properties. Previous studies, such as those from the ODISEA Atacama Large Millimeter/submillimeter Array (ALMA) survey (L. A. Cieza et al. 2019), classify ISO-Oph 37 as a young, disk-bearing YSO with a disk inclination of ∼72°, consistent with its flat-spectrum SED. Earlier near-IR surveys by T. P. Greene et al. (1994) also identify ISO-Oph 37 as a flat-spectrum source, though later classifications (S. Bontemps et al. 2001) mark it borderline Class II, underscoring its ambiguous evolutionary status. More recent and higher-sensitivity ALMA observations of its continuum confirm its high inclination (72.°6), and found evidence to classify it as a late Class I in evolutionary terms (M. Vioque et al. 2025). Its flat SED, high disk inclination, and classification uncertainties imply that ISO-Oph 37 is still relatively young (≲1 Myr old) and possibly retains some

Table 1
Source Properties

Property	Value	References
Spectral Type	K7	C. F. Manara et al. (2015)
L_{bol}	1.82 $L_\odot$	N. J. I. Evans et al. (2009)
T_{bol}	670 K	N. J. I. Evans et al. (2009)
α_{IR}	−0.01	N. J. I. Evans et al. (2009)
$M_\star$	0.6 $M_\odot$	D. A. Ruiz-Rodriguez et al. (2025)
R_{95}	104 au	M. Vioque et al. (2025)
Distance	138.4 pc	G. N. Ortiz-León et al. (2018)
A_v	16.1	C. F. Manara et al. (2015)
i	72.°6	M. Vioque et al. (2025)

envelope material (D. A. Ruiz-Rodriguez et al. 2025), likely transitioning between the embedded protostellar and more evolved T Tauri stages.

The JWST/MIRI spectrum of ISO-Oph 37, a solar-type source, reveals strong absorption by C_2H_2, HCN, CO_2, CH_4, and H_2O, while notably lacking detectable absorption from common ice species. We further complement the MIRI spectrum with high-resolution Keck/NIRSPEC observations of CO, providing additional kinematic and thermal constraints through the detection of both disk emission and an absorption component. Although its flat-spectrum classification and possible residual envelope suggest that the source is still young, the absence of ice absorption and the prominence of acetylene and methane more closely resemble the chemistry of more evolved, carbon-rich disks. This apparent mismatch between evolutionary classification and chemical inventory makes ISO-Oph 37 a valuable test case: it highlights the importance of geometry and local environment in shaping molecular spectra, and it suggests that the relationship between hydrocarbon abundance and disk age in solar-mass stars may be more complex than a simple evolutionary sequence. This paper is organized as follows. In Section 2, we describe the JWST/MIRI and Keck/NIRSPEC data acquisition and reduction. In Section 3 we outline the modeling of both datasets, and in Section 4, we present the results. In Section 5 we examine the origin of the absorption spectra, the carbon budget of the system, and the broader context of carbon evolution in planet-forming regions. Finally, our conclusions are summarized in Section 6.

2. Observations

2.1. JWST/MIRI-MRS

ISO-Oph 37 was observed with JWST/MIRI-MRS (M. Wells et al. 2015; I. Argyriou et al. 2023; G. S. Wright et al. 2023) on 2024 March 16 as a part of the GO 3034 program (P.I. K. Zhang) with all three MRS gratings and a total exposure of 455.1 s per sub-band. The spectrum was reduced with the JDISCS pipeline (v9.1; K. M. Pontoppidan et al. 2024) to maximize signal-to-noise ratio (S/N), reduce fringing, and improve the wavelength calibration. The details of the pipeline can be found in the original publication. Briefly, relative to the standard MRS pipeline (run through Stage 2b), we use the JDISCS pipeline to replace the default fringe/throughput calibration with an empirical spectral response function derived from an asteroid calibrator, yielding improved fringe removal and S/N. For v9.1, the 1.20.2 version of the JWST Calibration software is used (H. Bushouse et al. 2025), along with the jwst_1464.pmap Calibration Reference Data System context. The 1D spectrum is extracted with a wavelength-dependent aperture ($1.4 \times 1.22\,\lambda/D$) for each sub-band. The final extracted spectrum can be seen in Figure 1. Line images are generated by following the approach described in M. Narang et al. (2026). In short, the central point source is subtracted by a point-spread function (PSF) measured in six velocity channels adjacent to the line. To account for spatial drift in the PSF centroid as a function of wavelength, only PSF channels with similar centroid to the line are selected. The combined PSF is scaled to the peak of the flux of the central source in each wavelength channel before subtraction. This efficiently removes the wings of the PSF from extended structure. The zeroth moment line map is calculated by integrating over the full lines to <90% of the peak flux density.

The spectrum of ISO-Oph 37 exhibits a mix of emission and absorption features, with a particularly dense clustering of rovibrational water absorption lines between 5 and 8 μm. However, unlike typical protostars or more evolved disks seen edge-on (J. A. Sturm et al. 2023; W. R. M. Rocha et al. 2025), ISO-Oph 37 lacks strong H_2O or CO_2 ice absorption features. Instead, it shows only silicate absorption at 10 μm, suggesting that the line of sight predominantly samples warm material rather than cold envelope or disk midplane gas. The 12–16 μm region is also dominated by strong C_2H_2 absorption. At high column densities, emission from this molecule can form a pseudo-continuum, complicating the separation of gas and dust contributions (B. Tabone et al. 2023; J. Kanwar et al. 2024; T. Kaeufer et al. 2024). To avoid overestimating the C_2H_2 column density by assuming a specific contribution from the continuum, we implemented a two-part strategy for estimating the continuum, tailored to different wavelength regimes.

Outside the 12–16 μm region, we implemented the continuum-subtraction algorithm from K. Zhang et al. (2026), adapted from the empirical methods of K. M. Pontoppidan et al. (2024) and A. Banzatti et al. (2024). The continuum is determined by iteratively smoothing the spectrum over fixed wavelength intervals to trace the underlying dust emission and interpolating between continuum-dominated points to construct a smooth baseline. This approach removes broad dust features while preserving narrow gas lines, though in regions of dense line blending, it may subtract a small fraction of the gas signal. To mitigate this effect, we excluded specific intervals from the fit, namely, 7.55–7.75 μm, where CH_4 absorption is expected, and used different smoothing window sizes and numbers of iterations (i.e., the number of times the smoothing and interpolation are repeated) at short and long wavelengths.

For the 12–16 μm region, where the presence of C_2H_2 emission can significantly alter the apparent continuum, we simultaneously modeled the continuum and gas absorption using a third-degree spline function. This approach, detailed further in Section 3.1, ensures a more accurate recovery of the underlying dust continuum. The final continuum model across the full spectral range is shown in the inset of Figure 1 as the solid black line.

2.2. Keck/NIRSPEC

To account for the full reservoir of carbon and oxygen, we also include Keck/NIRSPEC observations of the 4.6–5.2 μm region covering multiple ^{12}CO and ^{13}CO transitions. High-dispersion M-band spectra were acquired over several epochs from 2023–2025 with the updated NIRSPEC2.0 cross-dispersed echelle spectrograph (I. S. McLean et al. 1998; E. C. Martin et al. 2018) on the Keck II Telescope in its adaptive optics mode, using R-band light from the central star. The total integration time on source was 144 minutes, over programs on 2023 June 24, 26, 27 (PID: C211; PI: G. Blake), 2023 July 11 (PID: H226; PI: J. Williams), 2024 April 18 (PID: C421; PI: G. Blake), and 2025 June 13, 14 (PID: H397; PI: A. Anderson). Conditions were generally clear, with K-band seeing ranging from 0.″4–1.″2 and an average precipitable water vapor (PWC) of 2 mm (and a total PWV range of 0.6–6 mm).

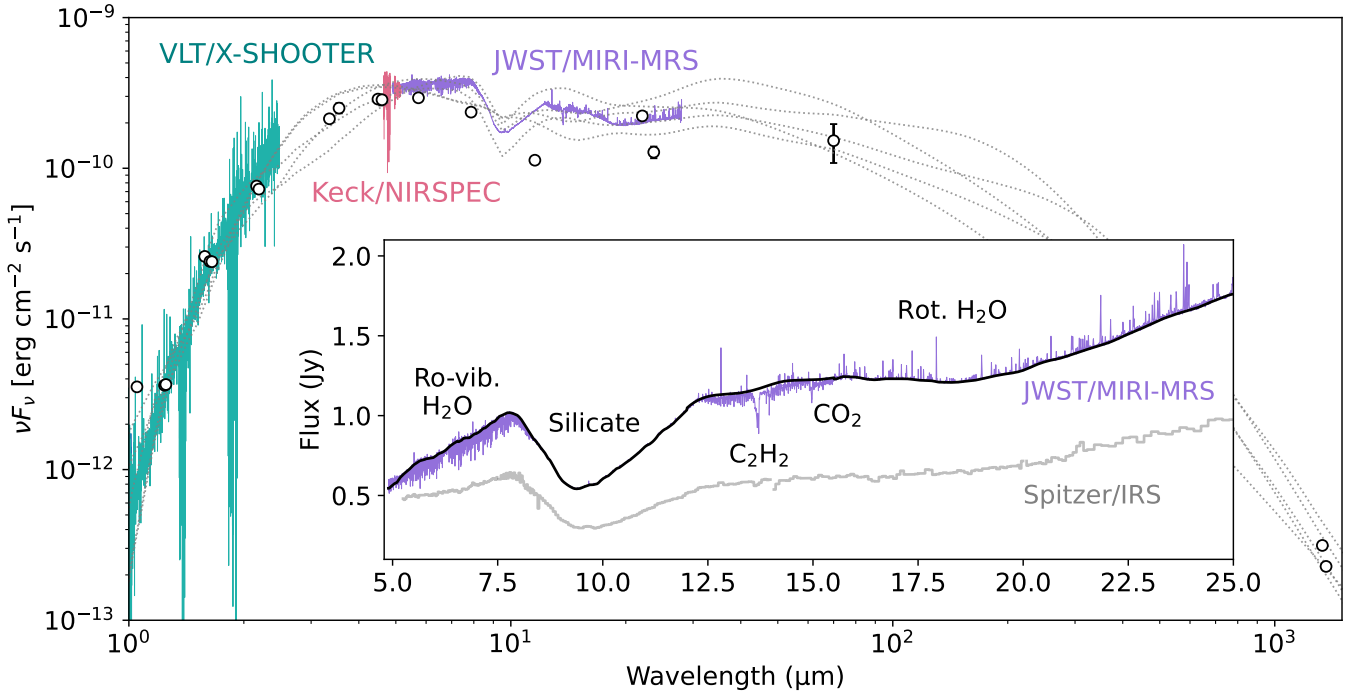

Figure 1. Spectral energy distribution (SED) of ISO-Oph 37. Photometric points are compiled from K. Zhang et al. (2025) and G. Marton et al. (2024). The X-SHOOTER spectrum is taken from C. F. Manara et al. (2015). The dotted gray lines show the best-fit SEDs, described in Appendix D. The inset shows the JWST/MIRI-MRS spectrum, and Spitzer/IRS spectrum taken from the CASSIS database (The Combined Atlas of Sources with Spitzer/IRS Spectra, CASSIS, is a product of the Infrared Science Center at Cornell University, supported by NASA and JPL; V. Lebouteiller et al. 2011), with some identified gas-phase features. The black line shows the inferred continuum. The shown SED is not corrected for extinction.

On all 2023–2024 nights, the 0.″027 × 2.″26 slit was used, yielding a resolving power of $R \sim 37{,}500$ (∼8 km s^{-1}), while those in 2025 used the 0.″041 × 2.″26 slit, which provided a resolving power of $R \sim 25{,}000$ (∼12 km s^{-1}). Because only a modest fraction of the full M-band window can be covered in a single echelle setting with NIRSPEC2.0, we use two echelle and cross-disperser settings to capture a wide range of CO lines with varying excitation energy, over a wavelength range of 4.64–5.16 μm, but with a gap from 4.85–4.95 μm.

We used an ABBA nodding pattern to facilitate the removal of sky and background fluxes we employed an ABBA nodding pattern, with each nod having a 1 minute exposure time. To enable searches for spectro-astrometric signatures in the disk CO gas, the spectrograph's slit was oriented parallel and antiparallel to the millimeter-disk's major axis at 48°/228° and along the disk minor axis at 138°/218° (L. A. Cieza et al. 2021). The bright star HR 5984 (β Sco, V4∼2.62 mag; spectral type B1V) served as the primary telluric standard, with maximum separations in airmass between the target and standard of 0.15, with a median separation of ∼0.06. Note that HR 5812 was chosen as the telluric standard for the 2024 April 18 data.

As described in A. R. Anderson et al. (2024), the data were reduced and calibrated using a processing pipeline that performs standard infrared data reduction techniques (i.e., flat-fielding, dark-subtraction, bad-pixel masking, A-B pair subtraction). Specifically, sequential A-B pairs from a given night that were oriented along the same slit position angle were stacked prior to wavelength calibration, standard-star division, and 1D extraction to increase the S/N of the target. These 1D spectra were extracted by fitting a polynomial to each trace in the 2D spectrum. Next, the Reference Forward Model, a line-by-line radiative-transfer model designed to simulate telluric infrared spectra (A. Dudhia 2017), was used to calibrate the wavelength/plate scale. The stacked A-B pairs so processed were then divided by the standard star's spectrum to remove telluric absorption features. Regions of the spectrum with a sky transmission value of <0.7 (as indicated by a normalized standard-star spectrum) were not included in our analysis to reduce the possibility of interpreting a telluric absorption feature as a spectral feature from the star/disk.

After wavelength calibration, the spectra were shifted to the stellar reference frame using an ISO-Oph37 radial velocity of −7.9 km s^{-1} (T. Sullivan et al. 2019) to perform the heliocentric velocity correction needed to bring all epochs into a common reference frame (including the Earth-induced shifts at the time of the observations). The full suite of data were stacked and weighted according to errors, and a spline fit was used to generate a continuum-subtracted spectrum. Finally, the total flux beyond 5 μm was fixed to that derived in the JWST-MIRI spectrum. The calibrated CO spectrum, along with the MIRI observations, are shown in Figure 2. Multiple transitions of ^{12}CO across two vibrational transitions, and multiple rotational transitions, are identified in absorption and emission, along with lines of ^{13}CO predominantly in absorption. We also detect a couple of rovibrational water lines, as discussed in Section 3.2.

3. Methods

3.1. MIRI Slab Modeling

We derived the physical parameters of the observed emission and absorption lines using local thermodynamic equilibrium (LTE) slab models. These models calculate the total optical depth of a line from an assumed excitation temperature (T_{ex}) and column density (N_{col}). For emission

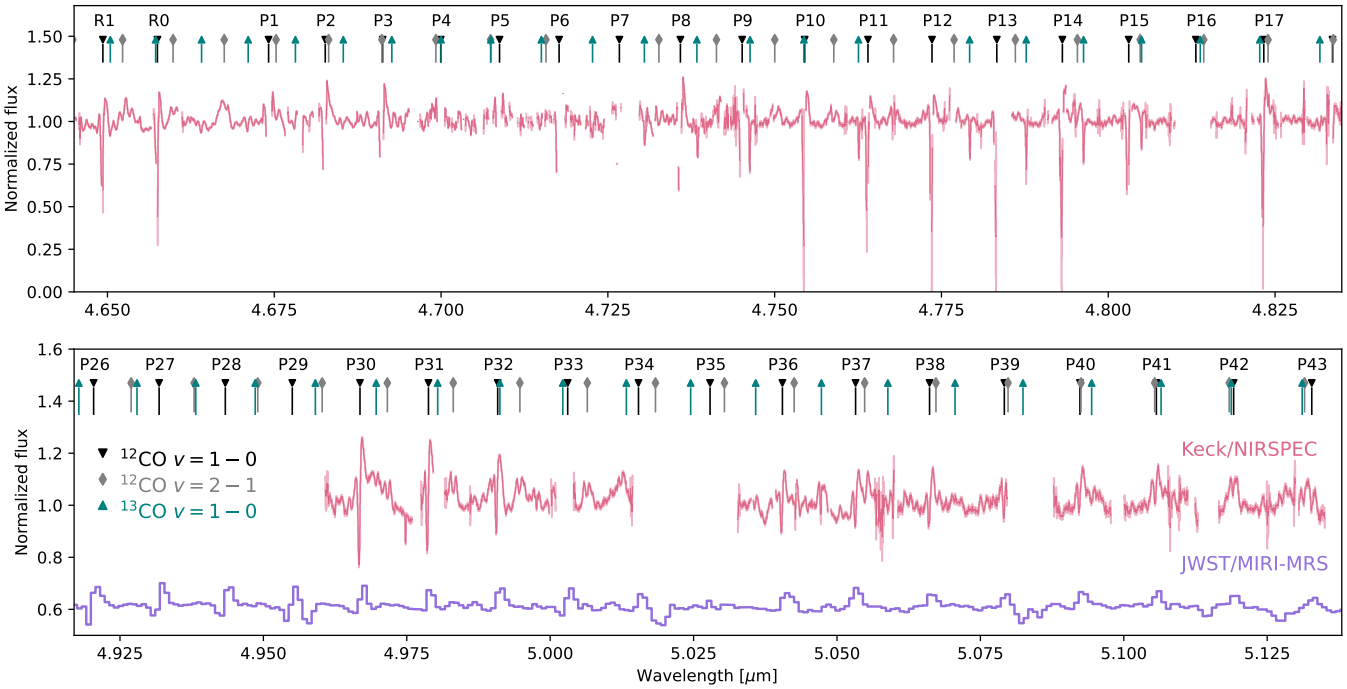

Figure 2. Observed CO lines in ISO-Oph 37. The pink line shows the Keck/NIRSPEC spectrum, and the purple line shows the JWST/MIRI-MRS data. The MRS spectrum is shifted down for clarity. Vertical lines and makers show the locations of the ^{12}CO $v = 1$–0 and $v = 2$–1, and ^{13}CO $v = 1$–0 lines. Labels denote individual ^{12}CO $v = 1$–0 rotational quantum numbers.

features, the observed flux can also be determined by assuming an emitting area ($A_{\rm em}$) and scaling the output to the source distance. LTE slab modeling has been extensively applied in the literature to extract physical parameters from both emission and absorption features (M. L. van Gelder et al. 2024a; N. Arulanantham et al. 2025; M. Temmink et al. 2025), and it has been shown that the retrieved parameters are usually in agreement with more complex thermochemical models (M. Vlasblom et al. 2025). Our observed spectrum contains a combination of emission and absorption components, requiring a region-by-region fitting strategy. Hence, we first separated the features into emission and absorption sets, and modeled them independently. Throughout this work, we generate the slab model spectra using the `spectools_ir` package (C. Salyk 2025), which uses molecular data from the HITRAN database (I. Gordon et al. 2026).

3.1.1. Emission

For the emission component, present beyond 15.5 μm, we adopt the same fitting algorithm as described in K. Zhang et al. (2026). Briefly, the slab models are computed in two MIRI/MRS wavelength intervals (15.5–18.8 and 18.8–27 μm), convolved to the corresponding MRS spectral resolution (A. Banzatti et al. 2024; K. M. Pontoppidan et al. 2024), and compared to the continuum-subtracted observed spectrum. We adopt a Gaussian likelihood, evaluated as the sum over the two spectral intervals,

$$\ln \mathcal{L}(\boldsymbol{\theta}) = -\frac{1}{2}\sum_{k=1}^{2}\sum_{\lambda_i \in [\lambda_{k,\min},\lambda_{k,\max}]}\left[\frac{F_{\rm obs}(\lambda_i) - F_{\rm mod}(\lambda_i|\boldsymbol{\theta})}{\sigma_{\rm obs}(\lambda_i)}\right]^2, \quad (1)$$

where $F_{\rm obs}(\lambda)$ is the continuum-subtracted spectrum (shifted by $v_r = -7.9\,{\rm km\,s^{-1}}$; T. Sullivan et al. 2019), and $F_{\rm mod}(\lambda|\theta)$ is the summed molecular slab model in the same interval, evaluated at the observed wavelengths. The set of molecules included in $F_{\rm mod}$ is allowed to differ between intervals, and Table 2 lists what wavelength interval was used for each species. Here, $\sigma_{\rm obs}$ represents the flux uncertainty of the observed spectrum, for which we adopt uncertainties of 2.5, 5, and 8 mJy for the 15.5–20, 20–22, and 22–27 μm regions, respectively, as calculated from the flux standard deviation of line-free regions. The intrinsic line broadening of the slab models is assumed to arise from thermal motions and therefore varies with the temperature of each species. Rather than correcting the observation for extinction, we extinct the models before comparing them with the observed spectrum. Similar to other sources with absorption (M. L. van Gelder et al. 2024b), we use the absolute extinction law from M. McClure (2009), assuming $A_{\rm V} = 16$ (C. F. Manara et al. 2015). The posterior is sampled with an affine-invariant Markov Chain Monte Carlo (MCMC) ensemble sampler. We adopt uniform priors within the parameter bounds listed in Table 4. For the cold water component ($H_2O_{\rm cold}$), we additionally impose a Gaussian prior on temperature centered at $T_{\rm ex} = 200\,{\rm K}$ with $\sigma = 50\,{\rm K}$, while all other parameters retain uniform priors.

We initially adopted three H_2O slabs representing different temperature reservoirs (~200 K, 400 K, 900 K) that have been identified in the analysis of T Tauri stars (A. Banzatti et al. 2024). However, the hot water component contributed negligibly to the model flux and is therefore excluded from the final fit. We also detected highly excited OH emission between 9 and 11 μm, likely produced by H_2O photodissociation. This component, typically not in LTE, can also contribute to the OH emission observed at longer wavelengths. To account for these potential contributions, we used the OH

Table 2
Parameters from the Slab Model Fitting

Molecule	Line Type	$\log_{10}N_{\rm col}$ ($\rm cm^{-2}$)	$T_{\rm ex}$ (K)	f_c	$\log_{10}A_{\rm slab}$ ($\rm au^2$)	Fitting Range (μm)
OH—warm	Emission	$16.57^{+0.03}_{-0.03}$	$499.38^{+6.15}_{-6.99}$	⋯	$1.34^{+0.02}_{-0.02}$	15.50–27.00
OH—hot	Emission	$16.60^{+0.19}_{-0.42}$	$1582.79^{+298.00}_{-144.60}$	⋯	$-0.74^{+0.06}_{-0.05}$	15.50–27.00
H_2O—cold	Emission	$16.97^{+0.02}_{-0.02}$	$208.11^{+1.07}_{-0.99}$	⋯	$2.50^{+0.00}_{-0.01}$	18.8–27.00
H_2O—warm	Emission	$18.22^{+0.01}_{-0.01}$	$437.98^{+3.20}_{-0.25}$	⋯	$0.74^{+0.01}_{-0.01}$	15.5–27.00
H_2O	Absorption	$19.11^{+0.02}_{-0.02}$	$605.28^{+5.81}_{-5.19}$	$1.00^{+0.00}_{-0.00}$	⋯	4.91–9.00
CO_2	Absorption	$16.99^{+0.01}_{-0.02}$	$420.39^{+6.56}_{-3.96}$	$1.00^{+0.00}_{-0.01}$	⋯	12.00–16.00
C_2H_2	Absorption	$17.61^{+0.03}_{-0.02}$	$620.67^{+6.44}_{-2.70}$	$0.57^{+0.01}_{-0.02}$	⋯	12.00–16.00
^{13}CCH2	Absorption	$16.78^{+0.14}_{-0.08}$	$681.97^{+6.86}_{-5.64}$	$0.47^{+0.02}_{-0.02}$	⋯	12.00–16.00
HCN	Absorption	$16.60^{+0.03}_{-0.03}$	$461.79^{+10.79}_{-12.26}$	$1.00^{+0.00}_{-0.01}$	⋯	12.00–16.00
CH_4	Absorption	$18.42^{+0.04}_{-0.10}$	$550.25^{+46.96}_{-14.32}$	$0.59^{+0.03}_{-0.02}$	⋯	4.91–16.00
CO	Absorption	$18.34^{+0.56}_{-1.18}$	$962.19^{+568.75}_{-503.15}$	[1.00]	⋯	4.96–5.14

Note. The brackets indicate parameters that were fixed during the fitting.

models from B. Tabone et al. (2024) as a template and subtracted it from the 8.8–18 μm spectrum before performing the fitting. For the wavelengths longward of 15 μm, we expect the remaining OH emission to be in LTE. However, a single LTE OH component could not simultaneously reproduce the remaining features; therefore, we used two OH components, as in previous studies (e.g., K. R. Schwarz et al. 2024).

The H_2O and OH emission lines were simultaneously fit between 15.5 and 27 μm, with the cold H_2O component included only longward of 18.8 μm, where its contribution is expected to be strongest. We do not attempt to fit the CO lines detected with MIRI, as the profiles are a complex combination of emission and absorption. We instead perform the CO analysis on the NIRSPEC observation, detailed in Section 3.2. We run the MCMC fitting routine using 100 walkers and 10^4 steps to ensure convergence. We report the parameter values in Table 2, corresponding to the marginalized posterior medians (50th percentiles). Quoted uncertainties are the central 68% credible intervals (16th–84th percentiles).

3.1.2. Absorption

For the molecular absorption, present between 4.9–9 μm and 12–15.5 μm, we implemented two different fitting methods. Unlike in emission, there is no physically meaningful emitting area for absorption. Because the spatial distribution of the absorbing gas relative to the continuum source is generally unknown, we allow the absorber to cover only a fraction of the continuum. We account for this geometry by introducing a covering fraction f_c (J. Li et al. 2024), which is able to scale down the flux. The absolute flux can then be written as

$$F_\nu = F_c(1 - f_c(1 - e^{-\tau_\nu})) , \quad (2)$$

where F_ν is the absolute flux, F_c is the continuum flux, and τ_ν is the optical depth of the line. In the absorption slab model, τ_ν is computed self-consistently from the excitation temperature and column density of the gas, while the covering fraction f_c is treated as an additional free parameter. We note that while the covering fraction and column density can appear partially degenerate in the optically thin limit, this degeneracy is mitigated when multiple transitions spanning a range of excitation energies are considered. Increasing the column density does not simply deepen existing absorption features, but instead alters the relative strengths of transitions in the P, Q, and R branches. In contrast, varying the covering fraction primarily rescales the depth of all absorption features without changing the relative line ratios. As a result, models with high column density and low f_c cannot reproduce the observed line ensemble in the same way as models with lower column density and higher f_c. The simultaneous fitting of multiple transitions therefore provides independent constraints on $N_{\rm col}$ and f_c. To illustrate this point, we show in Figure 3 three representative absorption models with comparable line depths but different combinations of column density and covering fraction. Although the overall absorption strength is similar, the models differ in the relative strengths and presence of transitions across the P, Q, and R branches, demonstrating that the degeneracy between $N_{\rm col}$ and f_c is not global when multiple lines are considered.

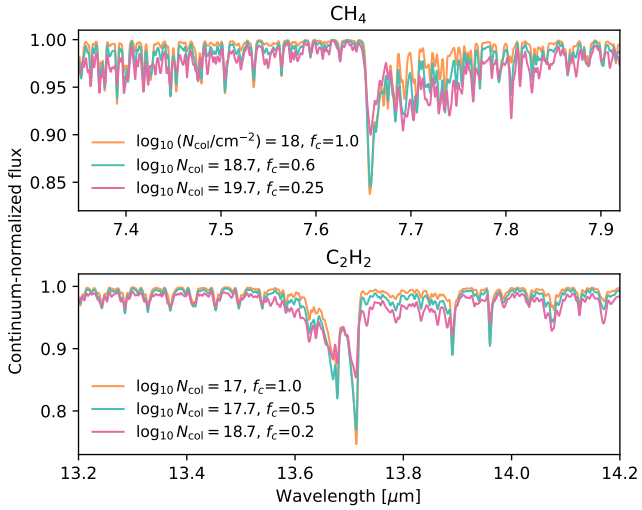

Figure 3. Comparison of the effect of the covering fraction f_c on the slab model spectra for CH_4 and C_2H_2. As the column density increases, the flux of the P branch also increases, while the Q branch flux decreases. All models assume $T_{\rm ex} = 500$ K.

The model spectrum that is compared to the observations is the absolute flux F_ν, constructed by multiplying the continuum-normalized absorption model by the continuum flux F_c. As a result, uncertainties in the continuum determination

propagate directly into the modeled absorption depths, making an accurate estimate of F_c essential for robust constraints on the parameters. Our continuum treatment is therefore chosen based on whether the local continuum can be reliably defined in the presence of broad absorption features, or whether such features prevent a priori continuum placement. In the shorter-wavelength region (5.5–9 μm), most of the rovibrational water and methane transitions occur at wavelengths shorter than 8 μm, where the spectrum is largely unaffected by the deep silicate absorption feature extending from ∼8–12 μm. We therefore adopt the pre-computed continuum derived from our continuum-subtraction algorithm described in Section 2.1 up to 12 μm.

In the case of the organics in the 12–16 μm range, the C_2H_2 absorption is abruptly "cut off" by the silicate absorption feature. In addition, because C_2H_2 is the strongest feature detected in our spectrum, we consider the possibility of a pseudo-continuum. When the column density of hydrocarbons is too high, these could saturate and create an optically thick pseudo-continuum that lies below an optically thin gas component, as has been observed in multiple hydrocarbon-rich sources (B. Tabone et al. 2023; A. M. Arabhavi et al. 2024; T. Kaeufer et al. 2024; J. Kanwar et al. 2024; H. Jang et al. 2025). This feature makes it difficult to correctly estimate a continuum. Therefore, instead of trying to establish a continuum before fitting the gas features, we remain agnostic to the continuum levels and simultaneously fit the gas features together with a spline function. We select eight equally distributed wavelength points between 12 and 16 μm, and estimate the continuum flux levels at each point by fitting a third-degree univariate spline function. Since the wavelength interval considered is relatively narrow, a third-degree spline provides sufficient flexibility to capture smooth continuum curvature while avoiding the introduction of artificial structure in the residuals. We also note that using a fourth-degree spline results in the same retrieved parameters. The eight selected points will create a continuum F_c, that is multiplied by each model before the likelihood function is evaluated. Therefore, the continuum is fit simultaneously with the C_2H_2, HCN, and CO_2 components, for which we vary the column density, temperature, and covering fraction. We also include a ^{13}CCH2 component, as it is commonly observed in systems with strong C_2H_2 (e.g., B. Tabone et al. 2023; A. M. Arabhavi et al. 2025). However, we include a condition in our prior that enforces the covering fraction and temperature to be within 10% of the values for C_2H_2, under the assumption that both species are roughly cospatial (see Appendix A for more details). The continuum and molecular absorption are therefore fit simultaneously, allowing the fit to accommodate a pseudo-continuum if present. The adopted parameter priors, spline node locations, and best-fit spline coefficients for this region are reported in Appendix A.

Similar to the algorithm implemented for emission, the fitting routines for absorption implement an MCMC algorithm to efficiently explore the parameter space, using 100 walkers and 10^4 steps. Uniform priors and physically motivated constraints are applied to all absorption model parameters, including temperature, column density, covering fraction, and continuum spline coefficients; the full prior specification is described in Appendix A. The resulting parameters and their uncertainties are obtained from the posterior distributions, and they are listed in Table 2. As in the emission analysis, we report posterior medians and 68% credible intervals. The resulting slab models are shown with the continuum-subtracted spectrum in Figures 4 and 5. We note that we only show the H_2O_{warm} model in the 12–16 μm region for reference, as it was not considered during the fitting of the absorption features.

3.2. Keck/NIRSPEC High-resolution CO Analysis

A significant fraction of the carbon and oxygen in disks can be locked in CO, so constraining its abundance is essential for characterizing the overall chemistry of the source. Because the spectral resolution of MIRI-MRS is insufficient to resolve the typically complex, multicomponent CO line profiles seen in disks (J. M. Brown et al. 2013; M. Temmink et al. 2024), and the MIRI wavelength coverage does not capture the full CO fundamental but rather just its tail, we complement the JWST data with high-resolution Keck/NIRSPEC observations of CO. The NIRSPEC profiles shown in Figure 2 display a combination of emission and blueshifted absorption. Since the absorption lines are visibly shifted by different velocities with respect to the rest velocity of the line transitions, a standard slab model fitting routine would struggle to minimize the residuals. Instead, we first construct an empirical, pure-absorption spectrum and then fit it with LTE CO slab models.

We modeled the rovibrational ^{12}CO absorption by first characterizing the line profile empirically and then fitting it with slab models. Starting from the continuum-normalized spectrum with associated uncertainties, we selected a set of relatively unblended ^{12}CO $v = 1$–0 and $v = 2$–1 lines from the HITRAN line list (I. Gordon et al. 2026) in the ranges 4.64–4.84 μm and 4.95–5.14 μm. For each line separately, we shifted the spectrum into the velocity frame of each transition and extracted a velocity segment around the line. We retained only those lines with adequate sampling of the absorption core and without obvious telluric contamination. For the $v = 2$–1 sample, we additionally rejected lines lying within 10 km s^{-1} of a $v = 1$–0 transition, as this latter one is expected to dominate. The retained per-line segments were combined into an inverse-variance-weighted stacked profile (including both the absorption and emission components), yielding an average line profile and corresponding uncertainty. Following the selection procedure, the retained $v = 1$–0 transitions included in the stacked profile are P(30)–P(32), P(36)–P(38), and P(40)–P(43), whereas the $v = 2$–1 stack consists of the P(26)–P(28) transitions. The stacked profiles, along with their 1σ uncertainty, are shown in Figure 6.

Then, the stacked profiles were modeled as the sum of a broad emission component and a narrower absorption component, approximated as

$$F_{\rm norm}(v) \simeq 1 + G_{\rm em}(v) - G_{\rm abs}(v), \quad (3)$$

where $F_{\rm norm}(v)$ is the continuum-normalized flux, and $G_{\rm em}$ and $G_{\rm abs}$ are Gaussians in velocity space, and each of these Gaussians is described as:

$$G(v;\ A,\ v_0,\ {\rm FWHM}) = A\ \exp\left[-4\ln 2\left(\frac{v - v_0}{\rm FWHM}\right)^2\right]. \quad (4)$$

In this parameterization, A is the Gaussian amplitude, defined relative to the continuum level of unity, such that $A_{\rm em} > 0$ produces an emission peak above the continuum, and $A_{\rm abs} > 0$ produces an absorption dip below the continuum. The parameter v_0 is the centroid velocity of the component relative

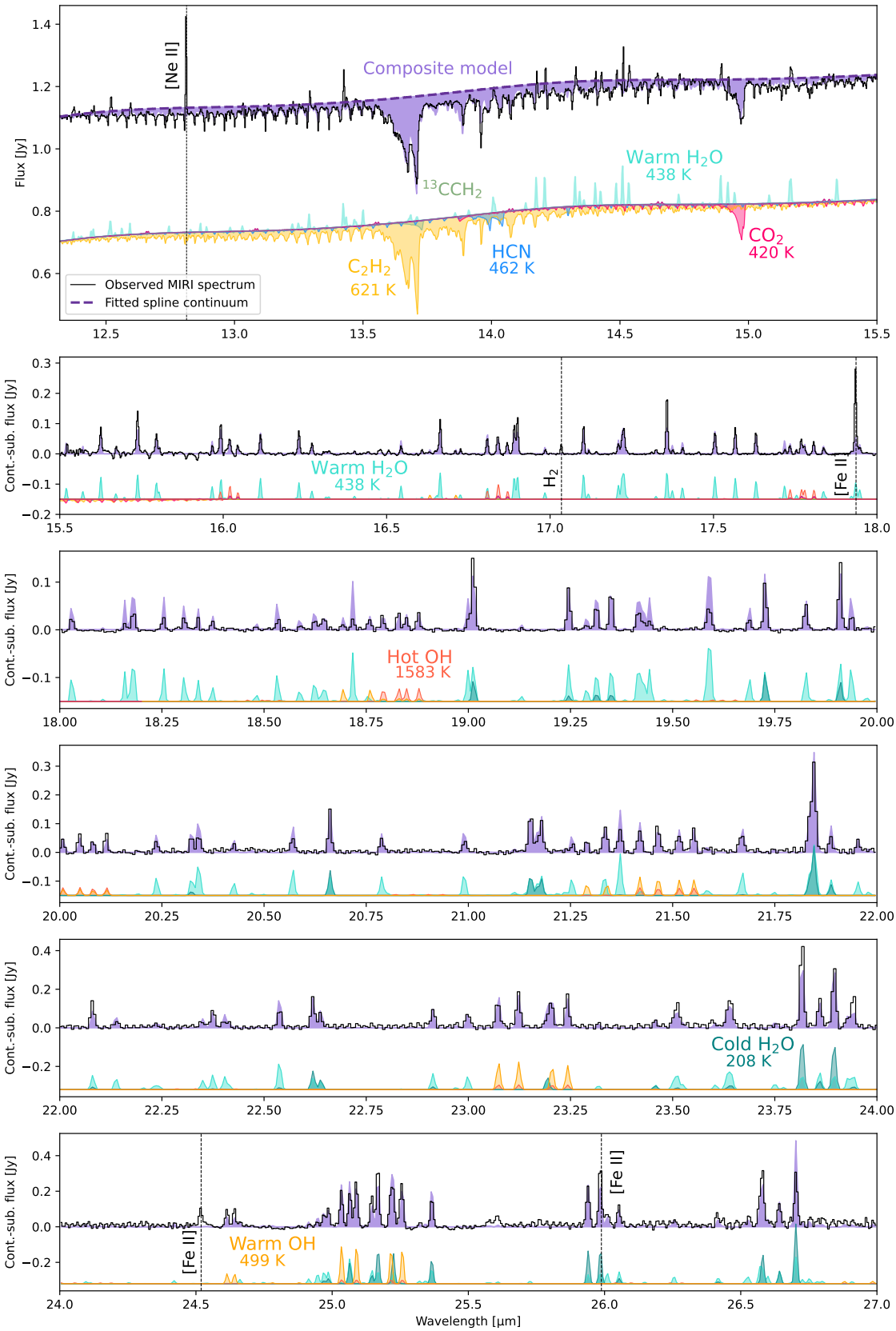

Figure 4. Best-fit LTE slab models beyond 12 μm. The top panel shows the absolute flux and the fitted continuum, whereas the rest of the panels show the continuum-subtracted flux. Molecular hydrogen and atomic lines are indicated with a vertical dashed line. The contribution from warm H_2O in the top panel is shown only for reference, as it was not used in the fitting procedure of the organics.

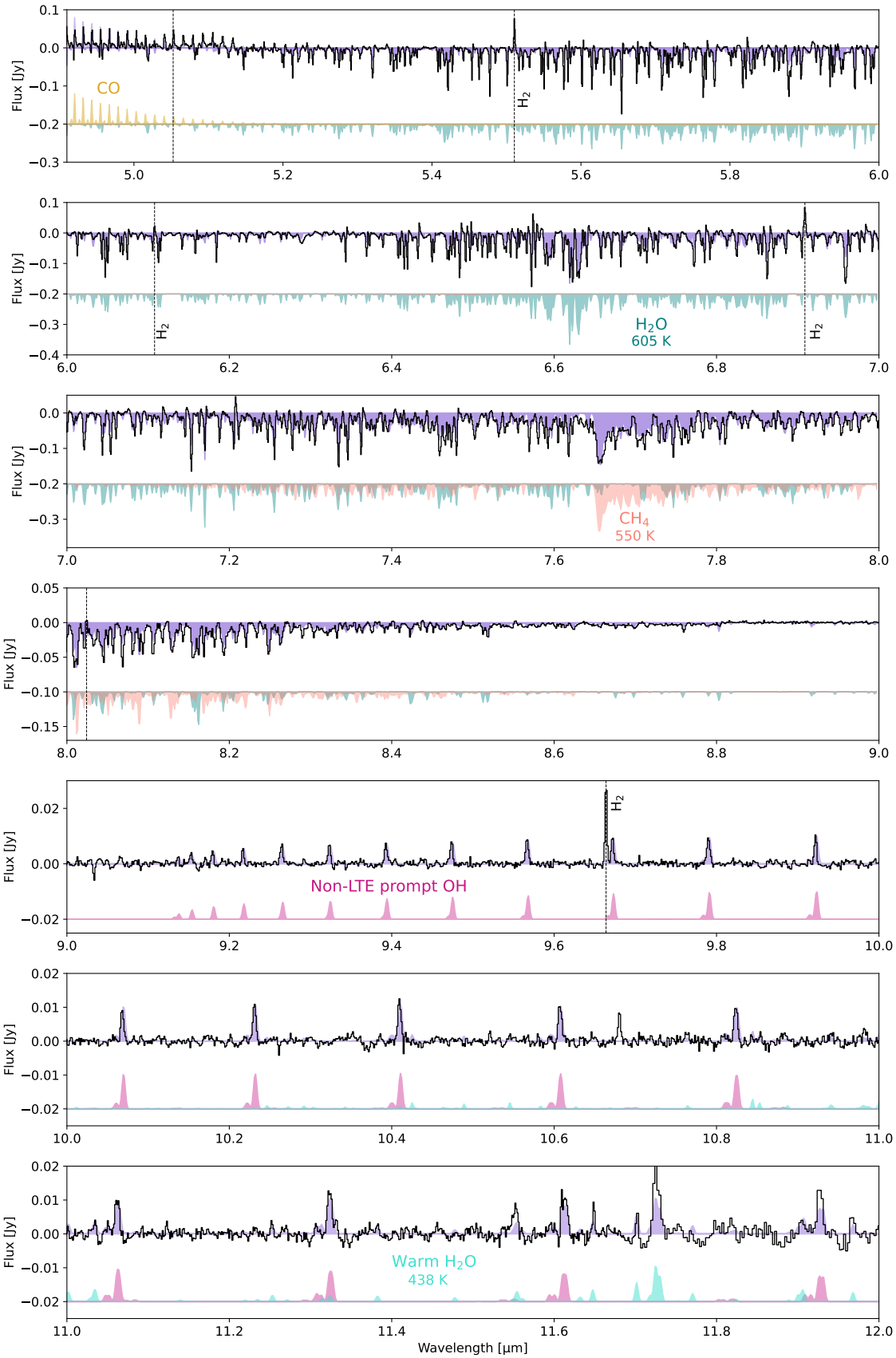

Figure 5. Best-fit LTE slab models between 4.91 and 12 μm. Molecular hydrogen and atomic lines are indicated with a vertical dashed line. The non-LTE prompt OH models are taken from B. Tabone et al. (2024). The warm H_2O models were reproduced from the best-fit parameters obtained for longer wavelengths, shown here just for reference. A CO model is shown just for reference.

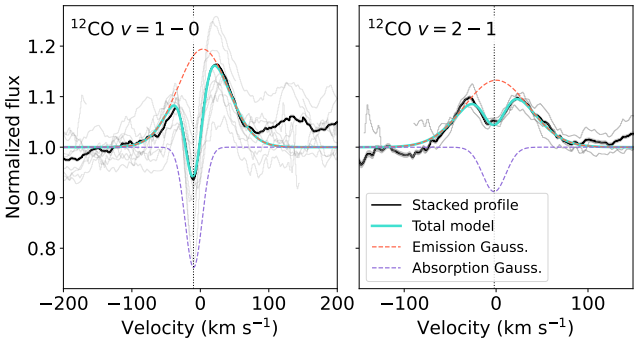

Figure 6. Stacked ^{12}CO profiles for the NIRSPEC observations. Light-gray lines show the individual profiles, while the black line shows the final stacked profile. The dotted vertical lines show the velocity centroid of the absorption component, v_0 from Table 3.

to the systemic velocity of the line. To avoid bias from the absorption core during the fitting of the Gaussians, we first fit the emission Gaussian only to the line wings, outside a chosen core interval around the line center. This emission Gaussian model was then used as a baseline; subtracting the emission from the stacked profile isolates a "dip" in the core, which we fitted with a second Gaussian to determine the absorption amplitude, centroid, and FWHM. This fitting procedure then results in two sets of parameters for the ^{12}CO $v = 1$–0 and $v = 2$–1 transitions. The parameter sets include FHWM of the emission and absorption Gaussians, their amplitudes, and their central velocities, listed in Table 3. The fitted Gaussians are shown in Figure 6.

As can be seen in the values for the best-fit Gaussians (Table 3), the absorption component of the $v = 1$–0 transitions is blueshifted by $\sim$10 km s^{-1} with respect to the system velocity, whereas the absorption in the $v = 2$–1 transitions is only blueshifted by $\sim$2 km s^{-1}. Given that the best spectral resolution achievable with our Keck/NIRSPEC observations is $\sim$8 km s^{-1}, the smaller blueshift measured for the $v = 2$–1 absorption is therefore only marginally resolved, while the larger blueshift of the $v = 1$–0 absorption represents a more robust, spectrally resolved offset. Furthermore, an absorption component not physically associated with the disk would not be expected to appear in higher vibrational transitions, as this would require very high excitation temperatures and column densities. We therefore interpret the $v = 2$–1 profiles as being dominated by the double-peaked line shape characteristic of Keplerian rotation in the disk, rather than tracing the same absorbing material seen in the $v = 1$–0 transition. Under this assumption, we estimate a characteristic Keplerian radius for the emitting gas from the FWHM of the emission Gaussian fitted to the $v = 1$–0 and $v = 2$–1 transitions according to

$$R_{\rm Kep} = GM_{\star}\left(\frac{\sin i}{\rm FWHM/2}\right)^2, \quad (5)$$

where M_* and i are the stellar mass and disk inclination, respectively, adopted from Table 1. The resulting radii are reported in Table 3.

Because the absorption seen in the $v = 2$–1 profile is unlikely to trace the same high-velocity absorbing material as the $v = 1$–0 lines, we restrict our subsequent analysis and column density determinations to the absorption observed in the $v = 1$–0 transition. To construct an empirical CO absorption spectrum that combines multiple lines, we first

Table 3
Best-fit Gaussian Parameters for the Stacked ^{12}CO Line Profiles

Transition	Component	A	v_0 (km s^{-1})	FWHM (km s^{-1})	$R_{\rm Kep}$ (au)
^{12}CO $v = 1$–0	Emission	0.1940	+3.52	86.19	0.26
...	Absorption	0.2381	−9.86	29.65	⋯
^{12}CO $v = 2$–1	Emission	0.1325	+0.32	82.70	0.28
...	Absorption	0.0881	−2.09	29.80	⋯

Note. The amplitudes A are dimensionless and defined relative to a continuum-normalized flux of unity. The centroid velocities v_0 are measured relative to the systemic velocity of the source.

adopt the emission and absorption FWHM values derived from the stacked profiles as global line widths applicable to all transitions.

With the line widths fixed, we then fit each individual line using a two-Gaussian model consisting of an emission and an absorption component, allowing only the amplitudes and centroid velocities of both components to vary. We limit this procedure to the subset of lines that were previously identified as suitable for inclusion in the stacked profiles.

From the set of successful per-line fits, we retain the absorption amplitudes and centroid velocities and reconstruct an empirical absorption-only spectrum over the full wavelength range by summing the Gaussian absorption contributions from all lines. This procedure yields a synthetic absorption flux spectrum, which we convert into an empirical optical-depth spectrum via

$$\tau_{\rm Gauss}(\lambda) = -\ln F_{\rm abs,norm}(\lambda), \quad (6)$$

where $F_{\rm abs,norm}(\lambda)$ is the continuum-normalized absorption flux.

Then, to infer the physical state of the high-velocity CO absorption component, we fit our empirical absorption-only spectrum with an LTE slab model. We adopted the observed FWHM of the absorption Gaussian (29.65 km s^{-1}; Table 3) as the FHWM for the convolution kernel in our slab models. This choice essentially reflects the fact that the observed FWHM is itself the convolution of the instrumental line-spread function and the intrinsic velocity dispersion of the absorbing gas. We performed an MCMC retrieval on $\tau_{\rm Gauss}(\lambda)$, comparing it to the model optical-depth spectra over the wavelength regions covered by the selected lines. The MCMC explores temperature and column density as free parameters, using the same general slab model framework as for the rovibrational water and CH_4 analysis described in Section 3.1, but fixing the covering fraction to $f_c = 1$. From the resulting posterior distribution, we adopt as "best-fit" parameters the maximum a posteriori (MAP) temperature and column density. Uncertainties are estimated from the marginalized posteriors as the 16th–84th percentile range. In this case, we choose to report MAP values rather than posterior medians primarily because the temperature posterior is non-Gaussian (see Appendix A), such that the median can fall in a relatively low-probability region. For the column density, the posterior is more sharply peaked, and the MAP and median are very similar; so this choice has a negligible effect. The resulting best-fit parameters are listed in Table 2, and the slab and overall modeled spectrum are shown in Figure 7. We note that we also detect ^{13}CO lines in the NIRSPEC spectrum. However, these lines

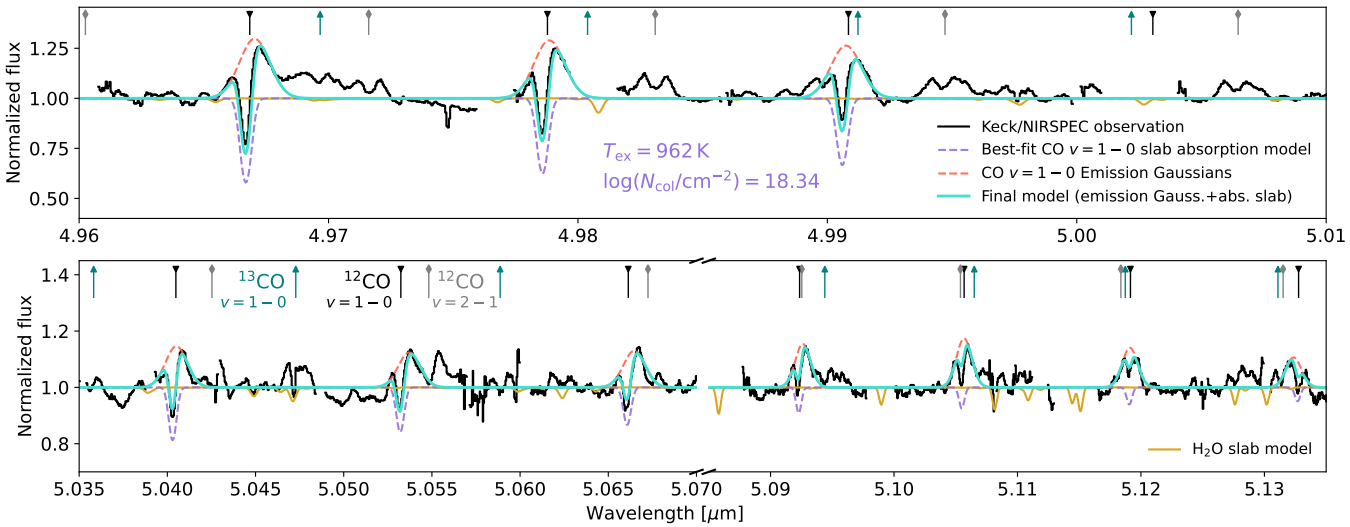

Figure 7. Resulting CO profiles from the LTE slab fitting. The purple dashed line shows the best-fit absorption slab model for the CO $v = 1$–0 transitions, and each line has been velocity shifted to match the absorption centroid. Transition line centers are shown for reference at the top. The ^{13}CO lines are analyzed in Appendix B. Some additional absorption features not associated with CO are consistent with water lines, using a slab model constructed with the same best-fit parameters derived from the MIRI observations (see the text).

are in pure absorption and trace a much colder (∼30 K) component, which is likely associated with a more extended envelope/cloud. We present the analysis of the ^{13}CO lines in Appendix B. Finally, some of the absorption features that do not correspond to CO are consistent with water lines. To investigate this, we generate a slab model using the best-fit parameters for the water absorption derived from the MIRI observations (Table 2) and convolve it to the Keck/NIRSPEC resolution. The resulting model is shown in Figure 7, where we find good agreement with several features, particularly near 5.045, 5.0625, and 5.128 μm. We do not pursue further analysis of these lines, as they are difficult to disentangle from overlapping emission, and the model already provides a satisfactory reproduction of the observed features.

4. Results

4.1. Absorption

Across the combined Keck/NIRSPEC and JWST/MIRI-MRS wavelength coverage, we detect six molecular species in absorption: CO, C_2H_2, HCN, CO_2, H_2O, and CH_4. Within the MIRI range, these species trace two distinct temperature components: HCN and CO_2 are associated with cooler gas (∼450 K), while C_2H_2, H_2O, and CH_4 trace warmer material (∼600 K). The best-fit column densities (log N/cm^2: C_2H_2 = 17.61, HCN = 16.60, CO_2 = 16.99, CH_4 = 18.46, H_2O = 19.13) place the source firmly within the "warm inner-disk" regime (N. Arulanantham et al. 2025). The CO absorption traces gas of comparable column density (log $N(CO)/cm^2$ = 18.07) but at significantly higher temperature (∼1000 K). This difference likely reflects the fact that the CO slab fitting relies on higher-energy transitions, as lower-energy lines that would probe cooler gas are strongly affected by telluric contamination. Although column density ratios can be derived from these measurements, the differences in temperature indicate that not all species necessarily arise from the same physical region. In particular, the higher excitation temperature of CO suggests that it may trace material located closer to the star than the species detected with MIRI. Accordingly, in the remainder of this work, we present ratios relative to CO for completeness but focus our interpretation on ratios involving species with comparable excitation temperatures (i.e., the rest of the species). Within this framework, we find that the absorbing gas is enriched in hydrocarbons, with $(C_2H_2+CH_4)/CO \approx 2$ and $(C_2H_2+CH_4)/HCN \approx 80$. In terms of the oxygen budget, most oxygen is stored in water, whose column density exceeds that of CO by an order of magnitude and that of CO_2 by nearly 2 orders of magnitude.

To place the results for ISO-Oph 37 in context, we compare our measurements with those of two other systems that exhibit well-characterized molecular absorption: IRS 46 and GV Tau N (Figure 8). Both sources are commonly classified as Class I; however, the absence of extended envelopes and their high inferred inclinations (∼75° for IRS 46 and ∼80° for GV Tau N) have led several studies to argue that they are more consistent with evolved, edge-on Class II disks (F. Lahuis et al. 2006; V. Roccatagliata et al. 2011; J. E. Bast et al. 2013; J. R. Najita et al. 2021). In this respect, these systems are closely analogous to ISO-Oph 37. Literature values for the column densities and excitation temperatures of IRS 46 are drawn from F. Lahuis et al. (2006) and J. E. Bast et al. (2013), while those for GV Tau N are compiled from E. L. Gibb et al. (2007), G. W. Doppmann et al. (2008), E. L. Gibb & D. Horne (2013), J. E. Bast et al. (2013), and J. R. Najita et al. (2021). In Figure 8, we present a comparative view of the molecular column densities, column density ratios, and excitation temperatures for all three sources. We note that these literature estimates are derived from heterogeneous observational datasets using Spitzer/IRS, Keck/NIRSPEC, and Gemini/TEXES, spanning spectral resolutions from $R \sim$ 600–100,000. As a result, the comparison is not strictly one-to-one, and systematic differences in wavelength coverage and modeling assumptions (e.g., continuum placement, line lists, line widths, and dilution) can shift inferred column densities and temperatures by factors of a few. Similarly, these systems are known to be variable (e.g., J. E. Bast et al. 2013; J. R. Najita et al. 2021); hence, the differences in column density might reflect the different observation epochs. When multiple literature values are available for a given species (i.e., HCN, C_2H_2, and CH_4), the absolute column density panel in

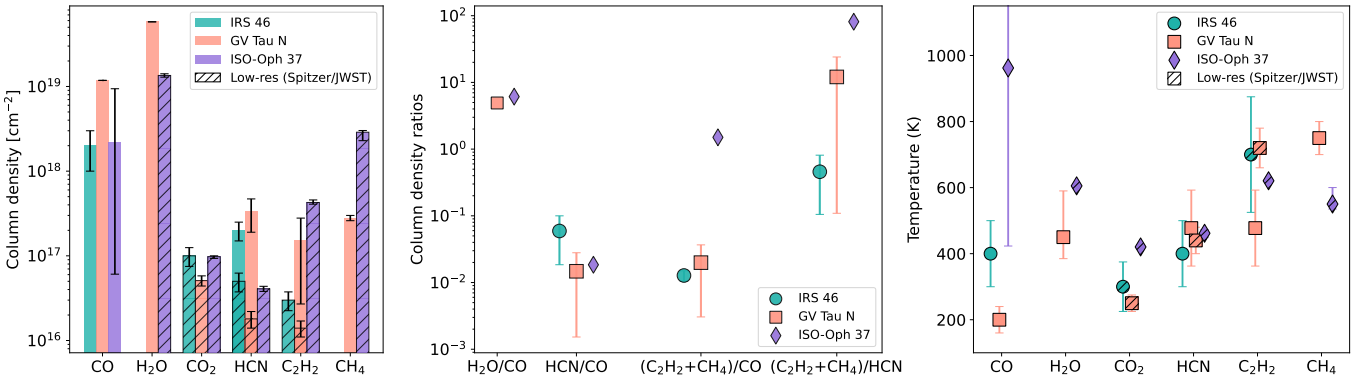

Figure 8. Comparison of molecular column densities and temperatures for ISO-Oph 37, IRS 46, and GV Tau N. When multiple literature values are available for a given source/species, the absolute column density panel shows the maximum reported value, corresponding to a best-case scenario for hydrocarbon richness. The temperature panel shows the excitation temperatures associated with these maximum column densities. The ranges shown in the column density ratio panel are obtained by combining the minimum and maximum reported column densities for each species, encompassing the diversity of observational constraints. Hatched regions indicate estimates using low-resolution observations.

Figure 8 shows the maximum reported value, corresponding to a best-case scenario for hydrocarbon richness. The temperature panel shows the excitation temperatures associated with these maximum column densities, highlighting the thermal conditions implied by the most hydrocarbon-rich interpretation of each source. In contrast, the column density ratio panel displays the full range of ratios permitted by the literature by combining the minimum and maximum reported column densities for each species, thereby encompassing the range of values inferred from heterogeneous datasets.

For ISO-Oph 37, the columns of HCN and CO_2 are comparable to IRS 46 and GV Tau N benchmarks (few $\times 10^{16}$–10^{17} cm^{-2}), whereas C_2H_2 and especially CH_4 are elevated for ISO-Oph 37 by $\sim$0.3–0.7 dex, pointing to a hydrocarbon-rich line of sight. This is more evident when comparing the C_2H_2 columns derived using the same lines (i.e., the ν_5 bending mode at 13.7 μm), as the Spitzer/IRS estimates for IRS 46 and GV Tau N are more than an order of magnitude lower than for ISO-Oph 37. Similarly, when comparing the column density ratios, even in the case where the highest reported C_2H_2 and CH_4 columns are assumed, the $(C_2H_2+CH_4)$/HCN values for both GV Tau N and IRS 46 are lower than $\sim$25, contrary to the $\sim$80 value found for ISO-Oph 37. This is also the case when comparing the $(C_2H_2+CH_4)$/CO ratio, as it is $\sim$100 times greater for ISO-Oph 37 than for the other two sources. In that context, the higher C_2H_2 and CH_4 either reflect an intrinsically carbon-rich chemistry or modest geometry/radiative-transfer effects. A practical caveat is that both C_2H_2 and CH_4 have covering fractions $f_c \sim 0.5$, whereas the other species have $f_c \sim 1$, meaning the latter are directly comparable to other studies, as they typically assumed $f_c = 1$; because covering fraction trades off with column density, ratios that mix "partial-covering" ($f_c = 0.5$, C_2H_2, CH_4) and "full-covering" ($f_c = 1$, HCN, H_2O) fits should be interpreted with this in mind. We refer the reader to the discussion of the covering fraction covered in Section 3. Among these organic species, the retrieved temperatures of ISO-Oph 37 are consistent with both sources.

The two most abundant oxygen carriers, CO and H_2O, have column density estimates that are consistent between ISO-Oph 37 and the other two sources, with CO typically being about a factor of 10 (10^{18} cm^{-2}) less abundant than water (10^{19} cm^{-2}), though we note IRS 46 lacks a water measurement. The main difference between sources for these species are the temperatures, with H_2O in ISO-Oph 37 being slightly hotter (600 K) than for GV Tau N (450 K), and CO being significantly hotter (1000 K) than GV Tau N (200 K) and IRS 46 (400 K). As mentioned before, this is likely due to the lines used in the slab model being sensitive to higher-temperature gas.

Overall, the absorption component of ISO-Oph 37 stands out as hydrocarbon-rich, with elevated C_2H_2 and CH_4 columns and ratios relative to IRS 46 and GV Tau N, despite comparable abundances of the dominant oxygen carriers. These characteristics point to distinct chemical conditions along the line of sight of the absorbing component.

4.2. Emission

In addition to the rich absorption spectrum described above, the MIRI/MRS data also reveal emission features that probe a distinct physical and excitation regime. At the shorter-wavelength end of the MIRI/MRS spectrum, we detect OH emission (see Figure 5). Unlike the nearly symmetric Λ-doublets expected for thermalized OH, only one component of each doublet is prominent. This is a feature of "prompt" OH produced when H_2O is photodissociated by FUV photons (often Lyα), leaving OH in highly excited, nonthermal states that radiatively decay before collisions can equilibrate the e/f parity levels (J. S. Carr & J. R. Najita 2014; L. Zhou et al. 2015; B. Tabone et al. 2024; M. Zannese et al. 2024). Because these lines are demonstrably out of LTE, we do not derive LTE column densities for OH; instead, we compare the observed doublet asymmetries and line ratios to published prompt OH models (B. Tabone et al. 2021, 2024). The presence of prompt OH emission points to gas exposed to an enhanced UV radiation field (D. A. Neufeld et al. 2024), whose implications for the disk chemistry we discuss in Section 5.

Longward of $\sim$15 μm, we also detect two OH rotational components characterized by distinct excitation temperatures ($\sim$500 K and $\sim$1600 K). The warm component is colder than typically seen in T Tauris (e.g., C. Salyk et al. 2011; D. Gasman et al. 2023), but it is similar to some species we see in absorption in this source (e.g., CO_2 and HCN), while the hotter OH likely traces more strongly irradiated or more interior disk layers.

For water, we identify two reservoirs in emission: a warm component at $\sim$440 K and a cooler component at $\sim$200 K,

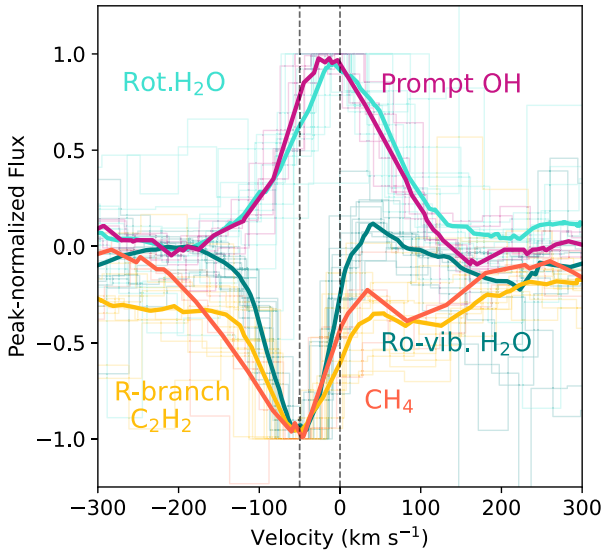

Figure 9. Stacked profiles of individual H_2O, C_2H_2, CH_4, and prompt OH transitions. The lines are in the velocity frame of the source (T. Sullivan et al. 2019). Dashed lines located at 0 and $-50\ km\ s^{-1}$ show the blueshift of the absorption component.

consistent with trends in T Tauri disks from Spitzer and JWST surveys (C. Salyk et al. 2011; N. Arulanantham et al. 2024). We do not find evidence for a hot ($\geqslant$800 K) water emission component reported in some systems (A. Banzatti et al. 2024; M. Temmink et al. 2025; C. E. Romero-Mirza et al. 2024), only the $\sim$600 K absorption component; the absence of hot water emission here could reflect efficient photodissociation in the innermost disk surface. Alternatively, the large inclination (74°) could be affecting our ability to trace the innermost disk surface, where the hot water component might reside.

4.3. Line Shifts

In previous pre-JWST studies of sources exhibiting molecular absorption, such as GV Tau N and IRS 46, velocity shifts relative to the stellar systemic velocity were reported and interpreted as key diagnostics of the absorption origin. Motivated by these results, we assess whether comparable velocity shifts are present in ISO-Oph 37. The details of the line selection used for this analysis, including the specific transitions and selection criteria for each species, are described in Appendix C.

Once the lines are selected in the spectrum, we subtract the previously determined continuum and shift the spectrum to the source rest frame using a systemic radial velocity of $-7.9\ km\ s^{-1}$ (T. Sullivan et al. 2019). For each selected transition, we convert the spectrum to velocity space around the line center, normalize each line segment by its local peak or trough, and interpolate onto a common velocity grid. We then compute the median of these normalized profiles to construct stacked-line profiles for each species, which are used to compare their characteristic line velocity centroids. The individual lines and stacked profiles are shown in Figure 9. From this, it is clear that the central velocities of the C_2H_2, CH_4, and H_2O in absorption are blueshifted up to $50\ km\ s^{-1}$ with respect to the H_2O and prompt OH in emission. We note that the smaller absorption peaks that seem to be redshifted, particularly in CH_4, could be due to contamination from adjacent lines, due to the difficulty of finding isolated line transitions. As noted in Appendix C, the CH_4 stacked profile only includes three lines. Previous velocity resolution estimates reached with the JDISCS wavelength calibration reported standard deviations of $4.4\ km\ s^{-1}$ at $<9\ \mu$m, $7\ km\ s^{-1}$ at 9–19μm, and $10\ km\ s^{-1}$ at $>19\ \mu$m (A. Banzatti et al. 2024), confirming our observed shift with $\sim 7\sigma$ confidence. For the ^{12}CO 1-0 data taken with NIRSPEC, the centroids of the fitted Gaussians for the absorption components shown in Figure 7 are all blueshifted, with velocities ranging from 4–15 $km\ s^{-1}$, significantly lower than measured in the MIRI-MRS observations.

In IRS 46, both the ^{12}CO and HCN lines were reported to be blueshifted by $\sim 25\ km\ s^{-1}$, under the assumption that the source itself is at the cloud velocity (F. Lahuis et al. 2006). These velocities were measured in Keck/NIRSPEC observations, which have a velocity resolution of $12\ km\ s^{-1}$. In contrast, the C_2H_2 and HCN lines of GV Tau N measured with TEXES ($3\ km\ s^{-1}$ resolution) showed redshifted absorption centered at around $4\ km\ s^{-1}$ with the red wing of the line extending up to 15–20 $km\ s^{-1}$ (J. R. Najita et al. 2021).

Taken together, the systematic blueshifts observed in the mid-infrared absorption lines, their clear separation from the emission components, and their consistency across multiple molecular species indicate that the absorbing gas is dynamically distinct from both the quiescent disk and the extended cloud environment. The contrast between the large blueshifts measured with MIRI and the more modest shifts seen in the near-infrared CO absorption further suggests that different tracers probe physically and geometrically distinct regions along the line of sight. These results point toward a structured inner-disk environment in which the absorbing material participates in an organized flow rather than purely Keplerian motion, motivating a closer examination of its physical origin in the context of disk winds. We further discuss the implications of these velocity shifts for the origin of the absorbing gas in Section 5.

4.4. Extended Emission

To characterize the observed geometry of the source, we analyze multiwavelength images. The source has been observed with ALMA both in ODISEA (as ISO-Oph 37; L. A. Cieza et al. 2019, 2021) and in AGE-PRO (as Oph 1/SSTc2dJ162623.6−242439; K. Zhang et al. 2025; D. A. Ruiz-Rodriguez et al. 2025; M. Vioque et al. 2025). In ODISEA, ISO-Oph 37 is classified as a flat-spectrum protostar, and the 1.3 mm continuum, as shown in Figure 10, shows a highly inclined ($i = 72.^{\circ}4$), extended, and largely smooth disk at $\sim$4 au resolution, with only a subtle inflection point at $\sim$31 au (L. A. Cieza et al. 2021). This morphology is consistent with the broader ODISEA result that embedded and flat-spectrum disks typically lack prominent ring-gap substructure compared to more evolved Class II disks (L. A. Cieza et al. 2021). AGE-PRO Band 6 observations recover a consistent inclination ($i = 72.^{\circ}6$), but the improved sensitivity reveals residuals in the inner disk that may be associated with substructure such as a dust trap or a snowline (M. Vioque et al. 2025). In molecular gas, ISO-Oph 37 exhibits strong contamination of the optically thick ^{12}CO and ^{13}CO $J = 2$–1 lines by extended cloud emission associated to the source, whereas the optically thinner C^{18}O and C^{17}O isolate the Keplerian disk: blue- and redshifted lobes are recovered cleanly in these isotopologues (D. A. Ruiz-Rodriguez et al. 2025).

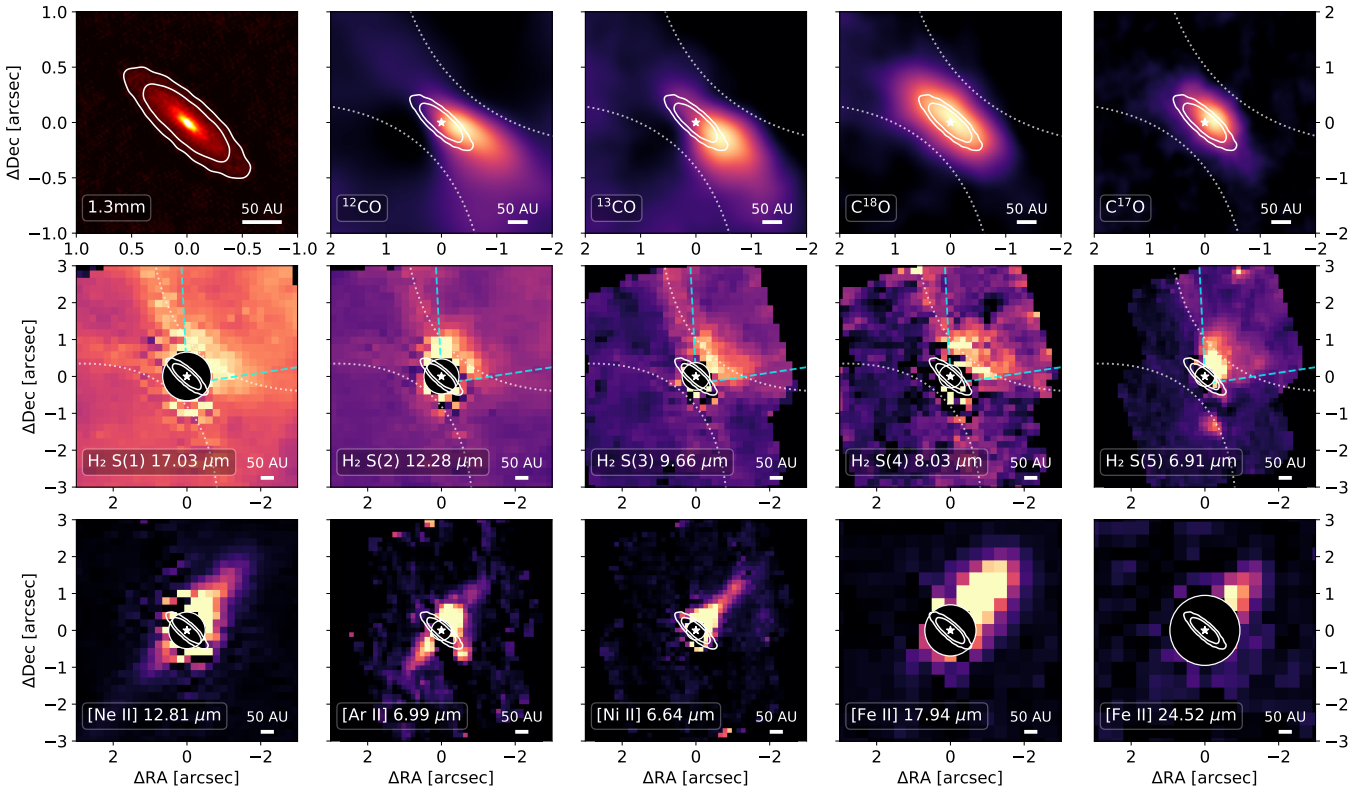

Figure 10. ALMA and JWST-MIRI images of ISO-Oph 37. Top row: ALMA 1.3 mm continuum image from ODISEA (L. A. Cieza et al. 2019), CO isotopologues from AGE-PRO (K. Zhang et al. 2025; D. A. Ruiz-Rodriguez et al. 2025). Dotted white lines show the disk surface, traced from the H_2 (S3) line emission from MIRI. Middle row: H_2 line images from MIRI. The black circle shows the inner working angle of JWST, and the contours show the 1.3 mm continuum from ALMA. Blue dashed lines show the disk wind, traced from the H_2 (S5) line emission. Bottom row: atomic line images from MIRI showing jet emission.

To place this emission in context, we generate line images of all pure rotational H_2 and selected atomic lines within the MIRI band. Pure rotational H_2 emission is commonly used to trace extended, low-velocity disk winds (A. R. Anderson et al. 2024; N. Arulanantham et al. 2024; I. Pascucci et al. 2025, K. R. Schwarz et al. 2025; M. Narang et al. 2026), while forbidden atomic lines are established tracers of high-velocity, collimated jets (Y.-L. Yang et al. 2022; M. Narang et al. 2024; E. F. van Dishoeck et al. 2025), and in some cases also winds (N. S. Bajaj et al. 2024). The resulting line images, overlaid with continuum contours, are shown in the bottom two rows of Figure 10.

The H_2 emission exhibits a complex, excitation-dependent morphology. Lower-excitation transitions show extended emission forming symmetric upper and lower lobes with a convex/concave appearance, most clearly traced by the H_2 S(3) line (outlined by the dotted white curves in Figure 10). The upper lobe is brighter, consistent with the high inclination of the system and partial obscuration of the far side. The orientation of this extended emission matches that of the $C^{17}O$ and $C^{18}O$ disk, suggesting that the lower-excitation H_2 primarily traces warm gas along the disk surface.

In contrast, higher-excitation H_2 emission, most notably the S(5) transition, appears more spatially confined and vertically collimated. This morphology closely resembles that observed in other systems hosting disk winds (A. R. Anderson et al. 2024; I. Pascucci et al. 2025), consistent with an origin in hotter gas launched close to the inner disk. The high-excitation H_2 emission is detected only on the upper side of the disk, mirroring asymmetries reported in other wind-hosting disks (N. S. Bajaj et al. 2025). The atomic lines trace an even more collimated component, oriented perpendicular to the disk. The [Ne II] and [Ar II] emission clearly delineate both the northern and southern jets, while [Ni II] predominantly traces the northern jet. This behavior is consistent with jet emission being stronger along the approaching flow direction and supports a nested morphology in which a fast, collimated jet is embedded within a slower, wider-angle wind, as seen in edge-on systems (I. Pascucci et al. 2025).

To further constrain the origin of the extended emission, we construct velocity maps from the MIRI cubes (Figure 11). As expected from the disk inclination and position angle, emission in the upper lobe is predominantly blueshifted, while the lower lobe is redshifted, both in H_2 and atomic lines. The H_2 emission associated with the upper-lobe wind exhibits velocities of 5–15 km s^{-1}, comparable to the blueshifted absorption velocities measured in the CO $v = 1$–0 line profiles (see Section 3.2). This kinematic agreement suggests that the mid-infrared H_2 emission and the CO absorption probe the same wind component. In contrast, the atomic lines trace substantially higher velocities ($\sim$60 km s^{-1}), characteristic of jet emission, most clearly seen in [Ne II] and [Ar II]. The [Ni II] and [Fe II] lines are detected only as blueshifted emission in the upper lobe, consistent with their spatial distribution in Figure 10. The presence of blueshifted CO absorption, extended H_2, and jets perpendicular to the disk, closely resemble what has been found in other systems such as CX Tau, where the observed components have been linked to a photoevaporative disk wind product of UV excitation (A. R. Anderson et al. 2024).

Overall, ISO-Oph 37 presents a dynamically layered environment in which a highly inclined disk is accompanied

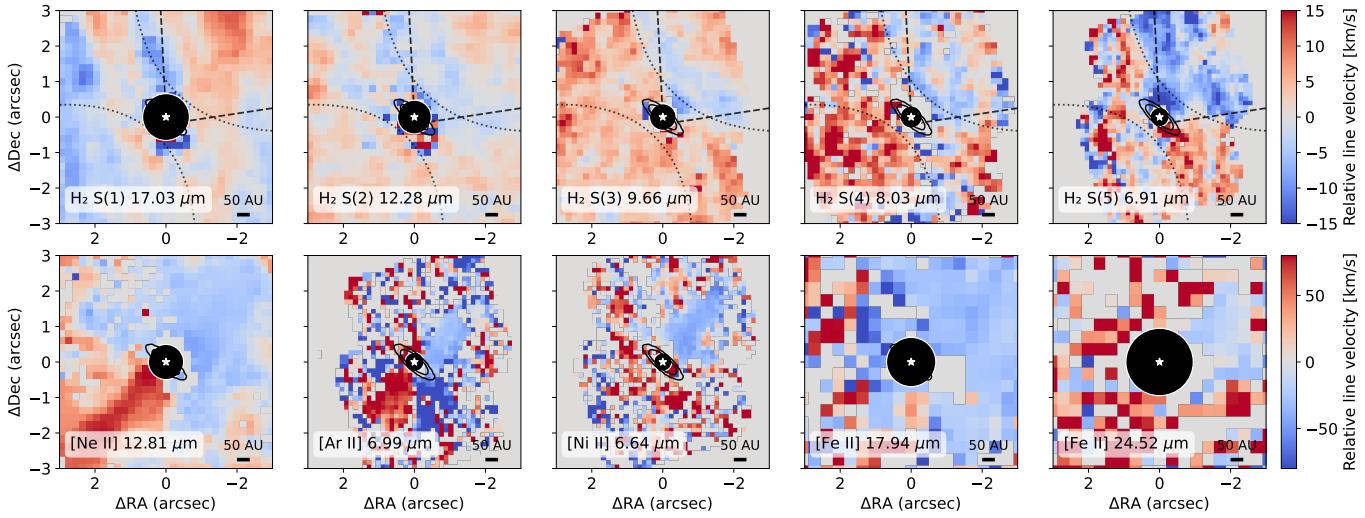

Figure 11. Line velocity maps of ISO-Oph 37. The top and bottom panels show the same MIRI lines as in Figure 10. Dotted black lines trace the disk surface inferred from the emission of the H_2 (S3) line, whereas black dashed lines show the disk wind opening angle traced from the H_2 (S5) emission. The solid black line show the 1.3 mm continuum from ALMA. The velocities are shown with respect to the source velocity of $v_r = -7.9$ km s^{-1}.

by both a slow, warm disk wind and a faster, collimated jet. The clear stratification in excitation, morphology, and kinematics across molecular and atomic tracers points to a nested structure linking the disk surface to progressively more energetic outflow components.

5. Discussion

Based on the results presented in the previous sections, we outline a schematic representation of our interpretation of the relative locations of the emission and absorption components observed in ISO-Oph 37. This schematic, shown in Figure 12, serves as a visual guide and is referenced throughout the discussion below. We note that the placement of molecular species along the wind is purely schematic and is intended to illustrate their inferred velocities, excitation temperatures, and covering fractions. It should not be interpreted as a chemical sequence or as implying in situ synthesis along the flow. Instead, all species are expected to be present in the inner-disk atmosphere and to be entrained in the wind, with their apparent spatial separation reflecting differences in kinematics and excitation rather than chemical evolution.

5.1. Origin of the Absorption

The excitation conditions and column densities of the absorbing gas strongly argue that the mid-IR absorption arises close to the inner disk rather than in the foreground cloud or a cold outer envelope. The hydrocarbons, CO_2, and HCN exhibit excitation temperatures of $T_{ex} \sim 400$–600 K, hotter than what is typically found in the envelopes of more-massive YSOs (D. An et al. 2011), and high columns (log $N/\mathrm{cm}^2 \sim 10^{16}$–$10^{19}$), far exceeding what is expected for quiescent cloud material. The absorbing layer must also lie very close to the continuum source; most species have covering fractions consistent with unity, while C_2H_2 and CH_4 require $f_c \approx 0.6$, suggestive of a partially filled line of sight where warm gas covers much, but not all, of the mid-IR continuum-emitting surface. In a highly inclined system ($i \sim 74°$), such partial covering naturally arises if the absorption originates in a geometrically thin but vertically extended structure, such as the base of a disk wind, rather than in a static, axisymmetric disk atmosphere.

Similar excitation conditions and molecular inventories have been reported toward IRS 46 and GV Tau, as both systems show mid-IR absorption from hot ($\gtrsim$350–700 K) organic gas located within the inner few astronomical unit and viewed at high inclination. In those systems, the absorbing material has been interpreted as originating either from the base of a disk wind (in the case of the blueshifted absorption in IRS 46; F. Lahuis et al. 2006) or from accretion flows along the disk surface (in the case of the redshifted absorption in GV Tau; J. R. Najita et al. 2021). These phenomena may represent different manifestations of the same underlying magnetically driven flow structure, as global nonideal MHD simulations (e.g., X.-N. Bai 2017) show that the inner disk can simultaneously host wind-driven outflows and surface accretion streams at different heights, with asymmetric magnetic field configurations naturally producing spatially distinct inflow and outflow components. This very dynamic environment is also consistent with the fact that the sources have shown variability on timescales of years (J. E. Bast et al. 2013; J. R. Najita et al. 2021).

In the case of ISO-Oph 37, we support a disk wind origin with a velocity- and temperature-stratified structure, based on the kinematic information. The MIRI C_2H_2 and H_2O absorption bands are blueshifted by 50 km s^{-1} relative to the systemic velocity, whereas the CO fundamental absorption observed with Keck/NIRSPEC is centered at only -10 km s^{-1} in the same frame. Such large velocity offsets are inconsistent with foreground cloud material in ρ Oph but are comparable to the blueshifts observed in near-IR molecular absorption toward IRS 46 (F. Lahuis et al. 2006).

Rather than indicating distinct physical origins for the different molecular species, we interpret these velocity differences as signatures of acceleration within a molecular disk wind. Gas launched near the base of the flow is expected to accelerate outward, so that material farther from the star can reach higher outflow velocities while cooling. The MIRI-traced species would then probe cooler, faster gas, whereas the CO absorption traced by the NIRSPEC lines reflects a hotter gas closer to the launching region that has not yet accelerated

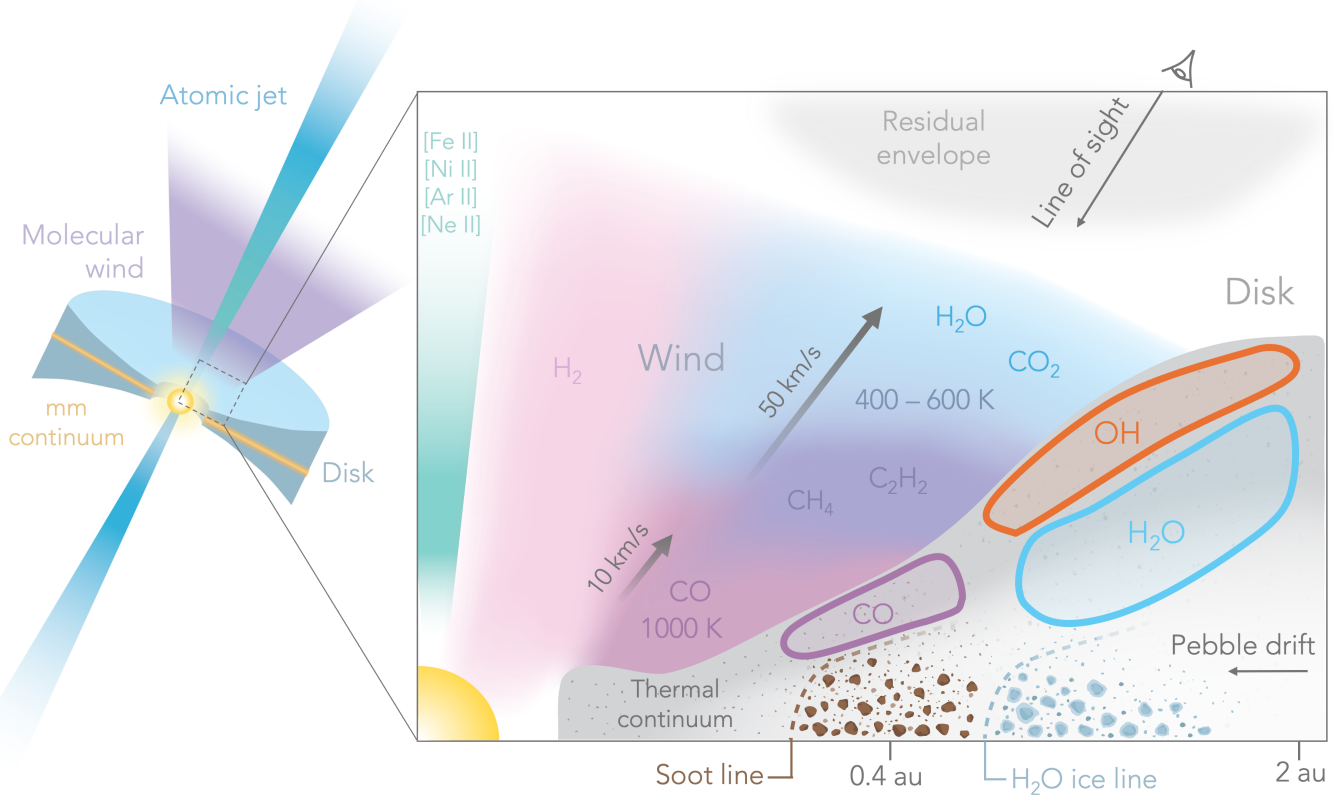

Figure 12. Schematic diagram of ISO-Oph 37. The thermal continuum serves as a background for some of the species in the wind (CO, C_2H_2, CH_4, H_2O, CO_2) to absorb against. The thick arrows show the direction of the wind velocity. The molecular labels in the wind are placed to indicate relative velocity, temperature, and covering fraction, and should not be interpreted as a chemical progression along the wind. All species are expected to originate in the inner-disk atmosphere and be entrained in the outflow. Solid contours show the species detected in emission.

to the higher velocities seen at larger distances, as represented in Figure 12. The presence of these organic species in a wind structure is also supported by the wind emission clearly observed in the H_2 lines.

The interpretation of a disk wind origin is consistent with magnetohydrodynamic (MHD) disk wind models, which predict acceleration and thermal stratification along the outflow (H. Shang et al. 2023; Y. Tu et al. 2025). The observed association of higher velocities with lower excitation temperatures in ISO-Oph 37 can therefore be explained within a single accelerating MHD wind, without invoking multiple unrelated components. Although the precise launch region of the outflow remains uncertain, its close spatial and kinematic association with the disk suggests that the absorbing gas is drawn from, or strongly coupled to, disk material. The molecular composition of the wind is therefore expected to broadly reflect that of the disk, rather than originating in a chemically distinct envelope component.

5.2. Evolutionary Stage

Several independent pieces of evidence point to ISO-Oph 37 being in a transitional evolutionary stage between an embedded protostar and a more settled Class II disk. Its low bolometric temperature (∼670 K) places it right at the edge of Class I/II classification (C.-H. Hsieh et al. 2025). Similarly, its SED has long been classified as flat-spectrum or borderline Class II (T. P. Greene et al. 1994; M. K. McClure et al. 2010; D. A. Ruiz-Rodriguez et al. 2025; M. Vioque et al. 2025), and the new MIRI spectrum presented here confirms a strong, rising mid-IR continuum attenuated by deep silicate features, indicative of substantial line-of-sight extinction. Nonetheless, it is known that high inclinations can make Class II objects appear as if they have an additional far-infrared excess from an envelope (T. P. Robitaille et al. 2006). Due to this degeneracy, we also explored the possibility of the inclination being the source of excess rather than the residual envelope. We modeled the full SED of the source, shown in Figure 1, using a grid of 180,000 synthetic SEDs designed for YSOs (T. P. Robitaille 2017; T. Richardson et al. 2024). These models cover a wide range of evolutionary stages by assuming different combinations of components (e.g., star, disk, envelope). The details of the modeling are presented in Appendix D; here, we only discuss the implications of the results, noting that the modeling is only meant to explain the overall behavior of the system rather than to find the "best-fit" parameters.

In the SED modeling, we find that the solutions that most closely resemble the observed SED do not uniquely prefer a purely disk-only solution: some models including a modest envelope and high viewing inclinations reproduce the broad-band SED about as well as disk-only configurations, also with high inclinations. This degeneracy between geometry (edge-on versus face-on) and evolution (embedded versus Class II) is a well-known limitation of SED-based classifications, especially in high-extinction regions such as ρ Oph where the mid-IR extinction law deviates from the ISM and can bias spectral indices (M. McClure 2009). This highlights the ambiguity of spectral index classifications, and the need to interpret the system integrating multiple observations.

In this context, the extended cloud emission detected in ^{12}CO and ^{13}CO may trace a low-mass remnant envelope associated with the early formation of the system (D. A. Ruiz-Rodriguez et al. 2025), pointing to a dynamically complex environment around ISO-Oph 37. Consistent with this picture, the AGE-PRO survey measured a dust radius of $R_{95\%} = 104$ au (M. Vioque et al. 2025), significantly larger than is typically observed for disks in Ophiuchus and notably lacking clear substructures (L. A. Cieza et al. 2019). In addition, ISO-Oph 37 hosts the second-highest gas mass in the AGE-PRO sample, with $M_{\rm gas} = 0.23\,M_{\odot}$ (L. Trapman et al. 2025). Taken together, these properties suggest that ISO-Oph 37 harbors a relatively massive disk that may still be embedded in, or partially surrounded by, a low-mass remnant envelope, rather than representing a fully exposed, evolved T Tauri disk. Another possibility is that the extended emission from ^{12}CO and ^{13}CO is tracing a large-scale streamer interacting with the disk, as has been proposed to explain the mid-IR emission in other systems (G. Perotti et al. 2026). However, the current data do not provide sufficient spatial or kinematic constraints to assess this scenario, and further observations of multiple molecular tracers on larger scales would be required to investigate this possibility.

At the same time, the molecular inventory of ISO-Oph 37 contrasts sharply with that of other young and embedded sources observed with JWST. While deeply embedded or edge-on systems at similar evolutionary stages commonly exhibit absorption dominated by ices formed at large radii (e.g., J. A. Sturm et al. 2024), the MIRI spectrum of ISO-Oph 37 is instead dominated by warm gas-phase absorption from C_2H_2, HCN, CO_2, CH_4, and H_2O, with excitation temperatures of $T_{\rm ex} \sim 400$–600 K. This places ISO-Oph 37 among the small subset of sources in which absorption traces warm inner-disk gas rather than cold envelope material, such as IRS 46 and GV Tau N (J. E. Bast et al. 2013; J. R. Najita et al. 2021).

However, even when compared to these sources, its spectrum is particularly rich in hydrocarbons, with prominent C_2H_2 and CH_4 absorption, pointing to carbon-rich conditions in the inner few astronomical unit. Although the absorbing gas is likely observed in an outflowing configuration, it must ultimately originate from disk material. The molecular absorption therefore reflects the composition of the inner disk at the point where gas is lifted into the wind, rather than that of a chemically distinct envelope. The presence of such a molecular inventory in a source that otherwise appears young and partially embedded indicates that substantial chemical processing of disk gas can occur early, before the system has fully evolved into a Class II disk, emphasizing that carbon-rich conditions might not be exclusive to system in later stages of their evolution (A. M. Arabhavi et al. 2025; F. Long et al. 2025).

5.3. Presence and Origin of Excess Carbon

The unusually high inferred $(C_2H_2{+}CH_4)/HCN$ column density ratio in ISO-Oph 37—and to a lesser extent the $(C_2H_2{+}CH_4)/CO$ ratio given the differences in excitation temperature—can be understood in at least two limiting scenarios. In the first scenario, the chemistry would be regulated by an increased UV radiation field; CO would be efficiently photodissociated in the presence of very strong UV, and the liberated carbon is subsequently processed into hydrocarbons through ion-molecule and high-temperature neutral–neutral chemistry, boosting the $(C_2H_2{+}CH_4)/CO$ ratio. This scenario would be partially supported by the presence of prompt OH emission in the MIRI spectrum, as it requires H_2O photodissociation. Nonetheless, both the absorption and emission components of H_2O still contain high columns of gas (see Table 2), indicating that the liberated oxygen might be reacting to reform H_2O faster than the FUV can photodissociate it. Similarly, the large H_2O columns inferred in both absorption would likely provide substantial self-shielding and mutual shielding of the wind material (T. Bethell & E. Bergin 2009), attenuating the FUV radiation field and making it difficult for UV photons to penetrate deeply enough to significantly deplete CO.

An alternative interpretation is that the CO and HCN abundances are typical for warm gas close to the inner disk, as suggested by the HCN/CO ratios, which are comparable to those measured in other sources (Figure 8), while the hydrocarbons, and to a lesser extent water, are enhanced. The expectation is that if most of the volatile oxygen is stored in water, the abundances reflect $H_2O/CO \approx 1.4$–2 (E. F. van Dishoeck et al. 2021). This makes the $H_2O/CO \approx 6$ found in ISO-Oph 37 unusually high, although in line with the estimate for GV Tau N (see Figure 8). This high H_2O/CO ratio could then be driven by an overabundance of water, which can be explained by a supply of H_2O icy pebbles (S. Krijt et al. 2025). Water abundances in the inner disk are expected to peak between 0.5 and 1 Myr due to the sublimation of water ice around inward drifting pebbles (A. Kalyaan et al. 2021, 2023; A. Houge et al. 2025b). Based on the relative incidence of different SED classes in nearby molecular clouds, N. J. I. Evans et al. (2009) estimated a statistical age of 0.9 Myr for the flat-spectrum phase, making the age of ISO-Oph 37 roughly correspond to the peak water abundance in the inner disk. In addition, the lack of gaps in the millimeter emission (L. A. Cieza et al. 2021; M. Vioque et al. 2025) suggests that there are no strong substructures or dust traps halting the drift of particles.

At the same time, the excess C_2H_2 and CH_4 could arise from the sublimation and thermal processing of carbonaceous grains at the soot line, where refractory carbonaceous material is destroyed, releasing volatile carbon into the gas phase (J. Li et al. 2021; M. J. Colmenares et al. 2024; A. Houge et al. 2025a). In this second scenario, the ratios we measure are signaling early and efficient redistribution of *both* oxygen and carbon reservoirs by pebble drift and soot-line chemistry, rather than a deficit of CO.

As discussed before, the differences in spectral resolution and coverage can affect the column densities estimated for each absorption system. Nonetheless, the HCN and C_2H_2 columns shown in Figure 8 that were inferred using the same wavelength coverage with IRS and MIRI-MRS, and that have similar temperatures across different systems, still point toward an excess of carbon in ISO-Oph 37, regardless of the CO content. This result then favors the carbon enhancement scenario due to the sublimation of refractory carbon grains. It is important to note that the excess carbon does not necessarily imply a high C/O ratio, as water is also found in high abundances. This is consistent with thermochemical models where excess oxygen from destruction of CO is driven to H_2O faster than CO can reform, and hence, the excess carbon produced from grain sublimation does not result in an elevated

C/O ratio despite the extra carbon being locked in hydrocarbon-chains (S. E. Duval et al. 2022).

More generally, this interpretation then has direct implications for the carbon reservoir available to forming planets. If refractory carbon is retained in solids, it can lead to the formation of carbon-rich ("soot-rich") planets (J. Li et al. 2026). On the contrary, if a significant fraction of the carbon in disks is released to the gas phase and subsequently entrained in a disk wind, then the inner disk may become depleted in solid-phase carbon before it can be incorporated into planetesimals, favoring carbon-poor terrestrial compositions. In this scenario, the same processes that lead to the observed hydrocarbon enhancements in the gas are simultaneously reducing the carbon available to build rocky planets. This system then provides a link between early pebble drift and carbon grain processing, to the carbon-poor composition of terrestrial planets like Earth, relative to their natal disk environments (J. Li et al. 2021).

6. Conclusions

We presented JWST/MIRI-MRS and Keck/NIRSPEC observations of ISO-Oph 37, a flat-spectrum source in the ρ Ophiuchi star-forming region. The spectrum reveals a combination of mid-infrared molecular absorption (CO, C_2H_2, CH_4, HCN, CO_2, and H_2O) and emission from CO, H_2O, and OH. By combining LTE slab modeling, spatially resolved line imaging, kinematic analysis, and SED modeling, we arrive at the following conclusions:

1. ISO-Oph 37 is best interpreted as a transitional system between an embedded protostar and a Class II disk. Its flat-spectrum SED, high inclination, smooth but moderately extended millimeter continuum, and large inferred gas mass are consistent with a massive disk that may still be partially embedded in, or interacting with, a low-mass remnant envelope. This evolutionary ambiguity highlights the limitations of SED-based classifications in highly inclined systems.
2. The JWST/MIRI spectrum reveals a rich molecular inventory that differs markedly between emission and absorption. Emission from H_2O and OH traces warm disk surface layers exposed to strong FUV irradiation, while the absorption spectrum probes warm gas close to the inner disk with $T_{ex} \sim 400$–600 K, dominated by C_2H_2, CH_4, HCN, CO_2, and H_2O. The high column densities inferred from absorption indicate that this gas lies close to the mid-infrared continuum source, within the inner few astronomical units.
3. The molecular absorption is kinematically distinct from the quiescent disk. The large blueshifts observed in the mid-infrared absorption lines (tens of kilometers per second), together with the more modest blueshifts detected in near-infrared CO absorption, rule out a static foreground or envelope origin. Instead, the velocity structure is consistent with a velocity- and temperature-stratified molecular disk wind, in which material launched from the inner disk accelerates outward. In this framework, the absorbing gas preserves the chemical imprint of the disk at the wind-launching region.
4. Compared to the benchmark absorption systems IRS 46 and GV Tau N, ISO-Oph 37 exhibits systematically enhanced C_2H_2 and CH_4 column densities and unusually high $(C_2H_2+CH_4)$/HCN and $(C_2H_2+CH_4)$/CO column density ratios. In contrast, the column densities of CO and HCN are comparable to those measured in the other absorption systems. These ratios therefore primarily reflect an overabundance of hydrocarbons rather than a deficit of CO and HCN.
5. The observed molecular ratios are most naturally explained by an enhancement of the inner-disk carbon reservoir rather than by UV-driven CO destruction. Inward drift and sublimation of icy pebbles can deliver excess H_2O to the inner disk, while sublimation and thermal processing of refractory carbonaceous grains at the soot line can efficiently recycle solid carbon into volatile hydrocarbons such as C_2H_2 and CH_4. In this scenario, the molecular disk wind acts as a tracer of disk chemistry, carrying an imprint of early pebble-driven redistribution of carbon and oxygen into the observed absorption spectrum.

ISO-Oph 37 thus demonstrates that carbon-rich inner-disk chemistry associated with pebble drift and soot-line processing can be established at relatively early evolutionary stages ($\lesssim$1 Myr) and be directly sampled through molecular absorption in disk winds. This loss of carbon-rich gas through disk winds may reduce the amount of carbon locked into solids in the inner disk, thereby affecting the composition of forming terrestrial planets. Absorption-selected systems like ISO-Oph 37 therefore provide powerful laboratories for linking disk chemistry to outflowing gas and for constraining how solid-phase carbon is recycled into the gas phase in planet-forming regions, a process that JWST is now uniquely positioned to explore across larger samples.

Acknowledgments

The authors thank the anonymous reviewer for providing suggestions, which helped improve the quality of the paper. M. J.C. thanks Nuria Calvet, Lee Hartmann, and August Masley for helpful discussions and guidance regarding the SED modeling presented in this work. S.K. and T.K. acknowledge support from STFC grant ST/Y002415/1. L.C. acknowledges support from ANID—Millennium Science Initiative Program —Center Code NCN2024_001. A portion of this research was carried out at the Jet Propulsion Laboratory, California Institute of Technology, under a contract with the National Aeronautics and Space Administration (80NM0018D0004). This work is based on observations made with the NASA/ESA/CSA James Webb Space Telescope. The data were obtained from the Mikulski Archive for Space Telescopes at the Space Telescope Science Institute, which is operated by the Association of Universities for Research in Astronomy, Inc., under NASA contract NAS 5-03127 for JWST. The JWST data is available at MAST: DOI: 10.17909/h1me-fk19. The W. M. Keck Observatory was made possible by the generous financial support of the W. M. Keck Foundation. We would like to thank all Keck Observatory staff who facilitated our observations. We recognize the cultural significance that the summit of Maunakea has within the indigenous Hawaiian community. We are deeply grateful for the opportunity to conduct observations from this mountain, while acknowledging the impact of our presence and the ongoing efforts to preserve this culturally and environmentally significant site.

This paper makes use of the following ALMA data:ADS/JAO. ALMA#2021.1.00128.L. ALMA is a partnership of ESO (representing its member states), NSF (USA) and NINS (Japan), together with NRC (Canada), MOST and ASIAA (Taiwan), and KASI (Republic of Korea), in cooperation with the Republic of Chile. The Joint ALMA Observatory is operatedby ESO, AUI/NRAO, and NAOJ. The National Radio Astronomy Observatory is a facility of the National Science Foundation operated under cooperative agreement by Associated Universities, Inc. We acknowledge the use of ChatGPT to assist with debugging code in the MCMC implementation and for minor language revisions to improve clarity and readability. All results were independently verified by the authors, and all scientific analyses and interpretations were conducted by the authors. The manuscript further benefited from language editing by all coauthors.

Facilities: JWST (MIRI), Keck II (NIRSPEC), ALMA.

Software: `numpy` (C. R. Harris et al. 2020), `scipy` (P. Virtanen et al. 2020), `Astropy` (Astropy Collaboration et al. 2022), `spectools-ir` (C. Salyk 2022), `emcee` (D. Foreman-Mackey et al. 2013), `sedfitter` (T. P. Robitaille 2017; T. Robitaille 2017), `ChatGPT` (OpenAI 2026).

Appendix A
MCMC Modeling Details

A.1. Emission

For the emission modeling, we adopt uniform priors on all slab parameters within physically motivated bounds, guided by previous analyses of mid-infrared molecular emission in disks (e.g., N. Arulanantham et al. 2025). The free parameters for each emitting component are the excitation temperature $T_{\rm ex}$, column density $N_{\rm col}$, and emitting area $A_{\rm em}$. The adopted prior ranges are listed in Table 4. To stabilize the decomposition of multiple water emission components, we impose an additional Gaussian prior on the excitation temperature of the cold water component, centered at $T_{\rm ex} = 200$ K with a standard deviation of $\sigma = 50$ K.

In addition, to promote rapid convergence of the MCMC sampling, walkers are initialized near representative starting values, listed as $T_{\rm ini}$, $\log N_{\rm ini}$, and $\log A_{\rm ini}$ in Table 4. These values are obtained by iteratively adjusting the parameters until the corresponding slab model provides a reasonable visual match to the observed spectrum. Importantly, these initial conditions are used solely to initialize the chains and do not affect the resulting posterior distributions, which are determined entirely by the likelihood function and the adopted priors.

Table 4
Priors Adopted for the Emission Slab Model MCMC Fits

Parameter	$H_2O_{\rm warm}$	$H_2O_{\rm cold}$	$OH_{\rm warm}$	$OH_{\rm hot}$
$T_{\rm ex,ini}$ [K]	450	200	400	900
$T_{\rm ex,min}$ [K]	200	100	100	100
$T_{\rm ex,max}$ [K]	800	400	1000	3000
$\log N_{\rm col,ini}$ [cm^{-2}]	18.2	17.0	17.5	16.0
$\log N_{\rm col,min}$ [cm^{-2}]	12.0	12.0	12.0	12.0
$\log N_{\rm col,max}$ [cm^{-2}]	22.0	22.0	22.0	22.0
$\log A_{\rm slab,ini}$ [au^2]	0.75	2.0	0.6	0.5
$\log A_{\rm slab,min}$ [au^2]	−2.0	−2.0	−2.0	−2.0
$\log A_{\rm slab,max}$ [au^2]	2.0	2.5	2.0	2.0

Table 5
Spline Node Wavelengths and Best-fit Continuum Fluxes (before Extinction) for the Absorption Modeling in the 12–16 μm Region

λ_j (μm)	$F_{c,j}$ (Jy)
12.0011	2.1747
12.5722	2.3143
13.1433	2.3248
13.7143	2.3701
14.2854	2.4441
14.8565	2.4433
15.4276	2.4518
15.9987	2.4992

A.2. Absorption

For the absorption modeling, we adopt uniform priors on the excitation temperature, column density, and covering fraction of each absorbing species:

$$T_{\rm ex} \sim \mathcal{U}(100,\ 1500)\ {\rm K},$$
$$\log N_{\rm col} \sim \mathcal{U}(16,\ 26)\ \ [{\rm cm}^{-2}],$$
$$f_c \sim \mathcal{U}(0,\ 1].$$

In the 12–16 μm interval affected by strong silicate absorption and potential hydrocarbon pseudo-continuum, the continuum is modeled simultaneously with the molecular absorption using a cubic spline. The spline is evaluated at a fixed set of node wavelengths λ_j, while the corresponding node fluxes $F_{c,j}$ are treated as free parameters with uniform priors,

$$F_{c,j} \sim \mathcal{U}(0.5,\ 3.0)\ {\rm Jy}, \quad j = 1,\ldots,8, \tag{A1}$$

ensuring positive and physically plausible continuum levels. We note that the continuum flux values $F_{c,j}$, as well as the best-fit continuum fluxes reported in Table 5, correspond to the dereddened flux levels. The spline-defined continuum is multiplied by the absorption model before comparison with the observed spectrum.

For isotopologues expected to trace the same absorbing gas reservoir, additional coupling constraints are imposed. In particular, the excitation temperature and covering fraction of ^{13}CCH2 are required to remain within 10% of the corresponding C_2H_2 values,

$$|T_{\rm ex}(^{13}{\rm CCH_2}) - T_{\rm ex}({\rm C_2H_2})| \leqslant 0.1\ T_{\rm ex}({\rm C_2H_2}),$$
$$|f_c(^{13}{\rm CCH_2}) - f_c({\rm C_2H_2})| \leqslant 0.1,$$

reflecting the assumption that both species arise from the same absorbing layer.

We include the posterior distributions for the CO slab modeling from Section 3.2 in Figure 13, showing that choosing the MAP over the median value for the CO column density results in an increase by a factor of ∼2 in column density. We emphasize that this result would not affect our overall conclusions, as the decrease in CO column density would only increase the (C_2H_2+CH_4)/CO ratio found for ISO-Oph 37, making it even more extreme than GV Tau N and IRS 46 (see Figure 8).

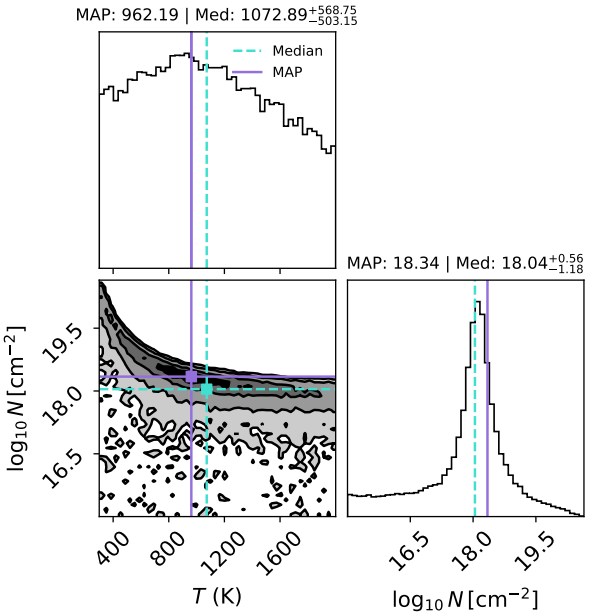

Figure 13. Posterior distribution from the MCMC slab model fitting for the CO $v = 1-$ absorption component.

Appendix B
^{13}CO in Keck/NIRSPEC Data

In addition to the ^{12}CO transitions detected in the NIRSPEC spectrum, we also detect the presence of ^{13}CO. To characterize the physical conditions of this gas, we perform a rotation diagram of all detected transitions that are separated by at least 10 km s^{-1} from a ^{12}CO line. Since the detected lines are only in absorption, we follow the methodology of previous works (e.g., J. Li et al. 2022) to derive a column density and an excitation temperature from the observed optical depth. We also build a stacked profile of the transitions to asses for bulk velocity shifts, following the procedure outlined in Section 3.2. We show the stacked profile, made up of transitions R(0), R(1), and P(1)–P(4) in Figure 14. Overall, the ^{13}CO lines seem to be tracing a much colder ($T_{\rm ex} \sim 30$ K) component, likely from the extended envelope seen in the ALMA images. This is also in agreement with the lack of a velocity shift, as seen in the stacked profile, and the fact that the line is seen purely in absorption.

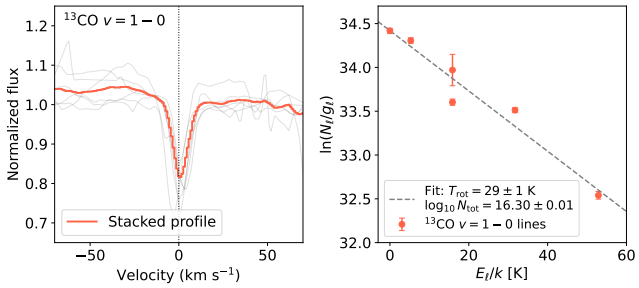

Figure 14. Left panel: ^{13}CO stacked profile. Gray lines show individual line transitions, and vertical dotted line shows rest velocity. Right panel: rotation diagram of ^{13}CO line absorption.

Appendix C
Line Selection for Velocity Shift Analysis

To search for velocity shifts in the molecular absorption and emission lines, we selected a set of unblended or minimally blended transitions for each species. For H_2O, we adopted unblended rovibrational and rotational transitions within the MIRI wavelength range from A. Banzatti et al. (2024). For C_2H_2, the absorption is dominated by relatively isolated R-branch features (see Figure 4). We therefore selected R-branch transitions from the HITRAN database in the 12.9–13.4 μm range with line intensities exceeding 10^{-19} cm^{-1} (molecule cm^{-2})$^{-1}$, yielding a total of 12 transitions. For absorption features, the HITRAN line intensity provides an appropriate metric for line selection, as it directly reflects the expected absorption strength under LTE conditions. For CH_4, which lies within a dense forest of H_2O absorption lines, we first identified wavelength regions where CH_4 transitions are relatively isolated from nearby H_2O features. Within these regions, we selected the transitions with the highest line intensities, resulting in three usable CH_4 lines. Finally, for the prompt OH emission, we searched the HITRAN database for candidate transitions near each detected feature in the 9.7–10.61, μm range that are not contaminated by H_2 or H_2O emission. Because prompt OH emission arises from nonthermal radiative decay following H_2O photodissociation, we selected, among the possible candidates, the transition with the highest Einstein A coefficient, which is expected to dominate the observed emission. The full list of selected transitions for each species is provided in Table 6.

Table 6
Wavelengths of Transitions Used in the Stacked-line Analysis

Species	Line Type	λ (μm)
H_2O (rot.)	Emission	15.62568
⋯	⋯	15.83495
⋯	⋯	15.96622
⋯	⋯	16.27136
⋯	⋯	16.50525
⋯	⋯	16.54402
⋯	⋯	17.10254
⋯	⋯	17.14148
⋯	⋯	17.19352
⋯	⋯	21.33317
⋯	⋯	22.37473
⋯	⋯	22.99881
⋯	⋯	24.05845
⋯	⋯	24.91403
H_2O (ro-vib.)	Absorption	5.34529
⋯	⋯	5.64107
⋯	⋯	6.07545
⋯	⋯	6.14316
⋯	⋯	6.18540
⋯	⋯	6.34443
⋯	⋯	6.43355
⋯	⋯	6.49224
⋯	⋯	6.52896
⋯	⋯	6.97738
⋯	⋯	6.99328
⋯	⋯	7.14692
C_2H_2 (R-branch)	Absorption	12.92418
⋯	⋯	12.96336
⋯	⋯	13.00280
⋯	⋯	13.04250
⋯	⋯	13.08246
⋯	⋯	13.12268
⋯	⋯	13.16317
⋯	⋯	13.20393
⋯	⋯	13.24495
⋯	⋯	13.28625
⋯	⋯	13.32781
⋯	⋯	13.36966
CH_4	Absorption	7.50344
⋯	⋯	7.97862
⋯	⋯	8.22233
OH	Emission	9.79069
⋯	⋯	10.06896
⋯	⋯	10.23102
⋯	⋯	10.40986
⋯	⋯	10.60681

Appendix D
SED Modeling

Infrared spectral indices are typically used to establish the evolutionary stage of young stellar objects (YSOs). However, many degeneracies between inclination, foreground extinction, and residual envelope emission can produce similar indices for physically distinct systems, motivating a complementary analysis based on full SED modeling. To explore this, we use a grid of pre-calculated SEDs for YSOs. These radiative-transfer models, first presented in T. P. Robitaille et al. (2006), have been recently updated and now include JWST observations (T. P. Robitaille 2017; T. Richardson et al. 2024), and have been widely used to characterize surveys of YSOs (e.g., M. Benedettini et al. 2018; N. Habel et al. 2024). In short, these models are made up of three components: a star, a disk, and an envelope, and they can include contributions from the ambient ISM, significant for line-of-sight extinction. The grid spans a broad range of stellar properties, disk and envelope masses, infall rates, cavity opening angles, and inclinations, and synthetic photometry is pre-computed for a large set of filters. For our fitting, we consider only the models that have a disk, but allow the ambient ISM and envelope to be optional. We use the photometry compiled in the AGE-PRO survey (D. A. Ruiz-Rodriguez et al. 2025; K. Zhang et al. 2025), and we calculate photometric fluxes for the MIRI filters from the MRS spectrum. To have a handle on the far-infrared excess, we take a Herschel/PACS measurement from G. Marton et al. (2024). However, as the flux for this observation was extracted $\sim$1.″5 away from the center of the source, we take this to be an upper limit on the surrounding envelope emission. During the fitting, we allow for an 80% confidence on the upper limit, which permits models to marginally exceed the measured flux while penalizing larger deviations through an increased χ^2 (see T. Robitaille 2017 for more details), thereby accounting for uncertainties in the spatial origin of the emission.

We fit ISO-Oph 37 using the `sedfitter` routine (T. Robitaille 2017; T. P. Robitaille 2017) with the updated models from T. Richardson et al. (2024), which compares the observed SED to this model grid. For each model, `sedfitter` scales the SED to the allowed distance range, applies a foreground extinction drawn from a specified A_V interval (in our case, $60 > A_v > 0$), and computes a χ^2 statistic using the observed fluxes and uncertainties. Models that require extreme scaling are rejected, and the remaining models are ranked by reduced χ^2. We show a subset of the fitted models in Figure 15. It is important to note that some of these models, even though they reproduce the emission, have parameters that are beyond the credible intervals, e.g., the stellar temperatures or intrinsic source luminosity are too high, the inclination is too low, etc. We emphasize that rather than adopting a single "best" model, the goal is to examine the ensemble of acceptable fits to assess whether disk-only configurations suffice or whether an additional envelope component is required, and to explore how inclination and extinction trade off in reproducing the observed SED. Therefore, we further select a subset of models that has stellar temperature, inclination, intrinsic source luminosity, and extinction within reasonable estimates of the values in D. A. Ruiz-Rodriguez et al. (2025) and M. Vioque et al. (2025), corresponding to $T_{\rm eff} = 3970$ K, $i = 72.^{\circ}59$, $\log L_\star = -0.06$, and $A_{\rm v} = 16.2$, respectively. These resulting models are shown as black lines in Figure 15.

Three of the best-fit models are matched with the `sp-h-i` models, which have contributions from a star and a passive disk, with the inner radius not fixed at the sublimation radius. The other two models correspond to configurations that include an envelope and ambient ISM. None of the models seem to prefer the configuration where the inner radius is set at the dust sublimation radius. Based on these five "best-fit" models, we can infer that the observed SED does not favor the absence or presence of an envelope, highlighting the evolutionary ambiguity of this source.

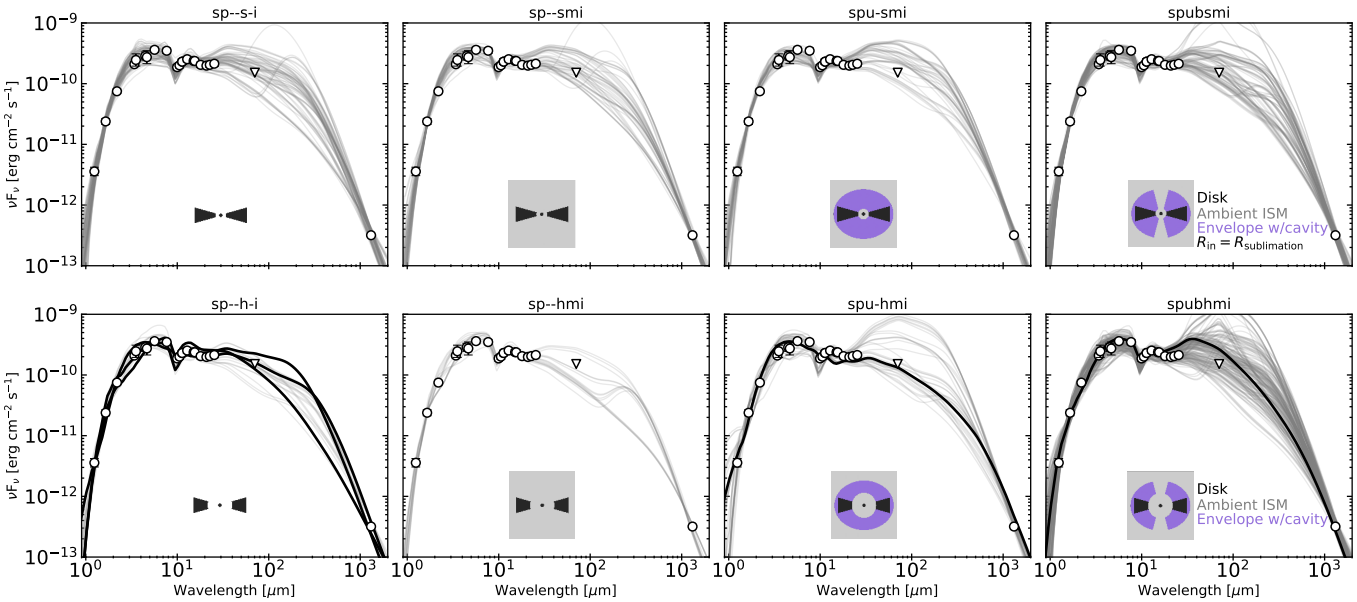

Figure 15. Best-fit SED models for ISO-Oph 37. Each panel shows a different model set, with the icon describing the contributions. Details on the specific model names are explained in T. P. Robitaille (2017).

ORCID iDs

María José Colmenares https://orcid.org/0000-0002-5296-6232
Edwin A. Bergin https://orcid.org/0000-0003-4179-6394
Ke Zhang https://orcid.org/0000-0002-0661-7517
Geoffrey A. Blake https://orcid.org/0000-0003-0787-1610
Klaus M. Pontoppidan https://orcid.org/0000-0001-7552-1562
Alexa R. Anderson https://orcid.org/0000-0002-4876-630X
John Carr https://orcid.org/0000-0002-6695-3977
Emma Dahl https://orcid.org/0000-0003-2985-1514
Joan Najita https://orcid.org/0000-0002-5758-150X
Jonathan P. Williams https://orcid.org/0000-0001-5058-695X
Colette Salyk https://orcid.org/0000-0003-3682-6632
Till Kaeufer https://orcid.org/0000-0001-8240-978X
Mayank Narang https://orcid.org/0000-0002-0554-1151
Ilaria Pascucci https://orcid.org/0000-0001-7962-1683
Benot Tabone https://orcid.org/0000-0002-1103-3225
Lucas Cieza https://orcid.org/0000-0002-2828-1153
Miguel Vioque https://orcid.org/0000-0002-4147-3846
Adrien Houge https://orcid.org/0000-0001-8790-9011
Sebastiaan Krijt https://orcid.org/0000-0002-3291-6887
Aditya M. Arabhavi https://orcid.org/0000-0001-8407-4020
Giovanni Rosotti https://orcid.org/0000-0003-4853-5736
John Carpenter https://orcid.org/0000-0003-2251-0602
Feng Long (龙凤) https://orcid.org/0000-0002-7607-719X
Paola Pinilla https://orcid.org/0000-0001-8764-1780
Jayatee Kanwar https://orcid.org/0000-0003-0386-2178
Eshan Raul https://orcid.org/0009-0002-2380-6683
Karina Mauco https://orcid.org/0000-0001-8284-4343
James Miley https://orcid.org/0000-0002-1575-680X
Abygail Waggoner https://orcid.org/0000-0002-1566-389X

References

An, D., Ramírez, S. V., Sellgren, K., et al. 2011, ApJ, 736, 133
Anderson, A. R., Williams, J. P., Blake, G. A., et al. 2024, ApJ, 977, 213
Arabhavi, A. M., Kamp, I., Henning, T., et al. 2024, Sci, 384, 1086
Arabhavi, A. M., Kamp, I., Henning, T., et al. 2025, A&A, 699, A194
Argyriou, I., Glasse, A., Law, D. R., et al. 2023, A&A, 675, A111
Arulanantham, N., McClure, M. K., Pontoppidan, K., et al. 2024, ApJL, 965, L13
Arulanantham, N., Salyk, C., Pontoppidan, K., et al. 2025, AJ, 170, 67
Astropy Collaboration, Price-Whelan, A. M., Lim, P. L., et al. 2022, ApJ, 935, 167
Bai, X.-N. 2017, ApJ, 845, 75
Bajaj, N. S., Pascucci, I., Beck, T. L., et al. 2025, AJ, 169, 296
Bajaj, N. S., Pascucci, I., Gorti, U., et al. 2024, AJ, 167, 127
Banzatti, A., Salyk, C., Pontoppidan, K. M., et al. 2025, AJ, 169, 165
Bast, J. E., Lahuis, F., van Dishoeck, E. F., & Tielens, A. G. G. M. 2013, A&A, 551, A118
Benedettini, M., Pezzuto, S., Schisano, E., et al. 2018, A&A, 619, A52
Bergin, E. A., Booth, R. A., Colmenares, M. J., & Ilee, J. D. 2024, ApJL, 969, L21
Bethell, T., & Bergin, E. 2009, Sci, 326, 1675
Bontemps, S., André, P., Kaas, A. A., et al. 2001, A&A, 372, 173
Brown, J. M., Pontoppidan, K. M., van Dishoeck, E. F., et al. 2013, ApJ, 770, 94
Brunken, N. G. C., van Dishoeck, E. F., Slavicinska, K., et al. 2024, A&A, 692, A163
Bushouse, H., Eisenhamer, J., Dencheva, N., et al. 2025, JWST Calibration Pipelin, v1.20.2, Zenodo, doi:10.5281/zenodo.17515973
Carr, J. S., & Najita, J. R. 2011, ApJ, 733, 102
Carr, J. S., & Najita, J. R. 2014, ApJ, 788, 66
Chapman, N. L., Mundy, L. G., Lai, S.-P., & Evans, N. J., II 2009, ApJ, 690, 496
Cieza, L. A., González-Ruilova, C., Hales, A. S., et al. 2021, MNRAS, 501, 2934
Cieza, L. A., Ruíz-Rodríguez, D., Hales, A., et al. 2019, MNRAS, 482, 698
Colmenares, M. J., Bergin, E. A., Salyk, C., et al. 2024, ApJ, 977, 173
Doppmann, G. W., Najita, J. R., & Carr, J. S. 2008, ApJ, 685, 298
Dudhia, A. 2017, JQSRT, 186, 243
Duval, S. E., Bosman, A. D., & Bergin, E. A. 2022, ApJL, 934, L25
Evans, N. J. I., Dunham, M. M., Jørgensen, J. K., et al. 2009, ApJS, 181, 321
Foreman-Mackey, D., Hogg, D. W., Lang, D., & Goodman, J. 2013, PASP, 125, 306

Furlan, E., Luhman, K. L., Espaillat, C., et al. 2011, ApJS, 195, 3
Gasman, D., van Dishoeck, E. F., Grant, S. L., et al. 2023, A&A, 679, A117
Gibb, E. L., & Horne, D. 2013, ApJL, 776, L28
Gibb, E. L., Van Brunt, K. A., Brittain, S. D., & Rettig, T. W. 2007, ApJ, 660, 1572
Gordon, I., Rothman, L., Hargreaves, R., et al. 2026, JQSRT, 353, 109807
Greene, T. P., Wilking, B. A., Andre, P., Young, E. T., & Lada, C. J. 1994, ApJ, 434, 614
Habel, N., Nally, C., Lenkić, L., et al. 2024, ApJ, 971, 108
Harris, C. R., Millman, K. J., van der Walt, S. J., et al. 2020, Natur, 585, 357
Houge, A., Johansen, A., Bergin, E., et al. 2025a, A&A, 699, A227
Houge, A., Krijt, S., Banzatti, A., et al. 2025b, MNRAS, 537, 691
Hsieh, C.-H., Arce, H. G., Maureira, M. J., et al. 2025, A&A, 700, A235
Jang, H., Arabhavi, A. M., Kaeufer, T., et al. 2025, A&A, 703, A53
Kaeufer, T., Woitke, P., Kamp, I., Kanwar, J., & Min, M. 2024, A&A, 690, A100
Kalyaan, A., Pinilla, P., Krijt, S., Mulders, G. D., & Banzatti, A. 2021, ApJ, 921, 84
Kalyaan, A., Pinilla, P., Krijt, S., et al. 2023, ApJ, 954, 66
Kanwar, J., Kamp, I., Jang, H., et al. 2024, A&A, 689, A231
Kanwar, J., Kamp, I., Woitke, P., et al. 2026, A&A, 705, A222
Krijt, S., Banzatti, A., Zhang, K., et al. 2025, ApJL, 990, L72
Lahuis, F., van Dishoeck, E. F., Boogert, A. C. A., et al. 2006, ApJL, 636, L145
Lebouteiller, V., Barry, D. J., Spoon, H. W. W., et al. 2011, ApJS, 196, 8
Li, J., Bergin, E. A., Blake, G. A., Ciesla, F. J., & Hirschmann, M. M. 2021, SciA, 7, 3632
Li, J., Bergin, E. A., Hirschmann, M. M., et al. 2026, ApJL, 997, L29
Li, J., Boogert, A., Barr, A. G., & Tielens, A. G. G. M. 2022, ApJ, 935, 161
Li, J., Boogert, A., & Tielens, A. G. G. M. 2024, ApJS, 273, 32
Long, F., Pascucci, I., Houge, A., et al. 2025, ApJL, 978, L30
Madhusudhan, N. 2012, ApJ, 758, 36
Mah, J., Bitsch, B., Pascucci, I., & Henning, T. 2023, A&A, 677, L7
Mah, J., Savvidou, S., & Bitsch, B. 2024, A&A, 686, L17
Manara, C. F., Testi, L., Natta, A., & Alcalá, J. M. 2015, A&A, 579, A66
Martin, E. C., Fitzgerald, M. P., McLean, I. S., et al. 2018, SPIE, 10702, 107020A
Marton, G., Gezer, I., Madarász, M., et al. 2024, A&A, 688, A203
McClure, M. 2009, ApJL, 693, L81
McClure, M. K., Furlan, E., Manoj, P., et al. 2010, ApJS, 188, 75
McClure, M. K., van't Hoff, M., Francis, L., et al. 2025, Natur, 643, 649
McLean, I. S., Becklin, E. E., Bendiksen, O., et al. 1998, SPIE, 3354, 566
Najita, J. R., Carr, J. S., Brittain, S. D., et al. 2021, ApJ, 908, 171
Narang, M., Manoj, P., Tyagi, H., et al. 2024, ApJL, 962, L16
Narang, M., Ohashi, N., Tobin, J. J., et al. 2025, AJ, 169, 192
Narang, M., Pontoppidan, K. M., Salyk, C., et al. 2026, submitted
Neufeld, D. A., Manoj, P., Tyagi, H., et al. 2024, ApJL, 966, L22
Öberg, K. I., & Bergin, E. A. 2021, PhR, 893, 1
OpenAI 2026, ChatGPT (GPT-5.3), https://chat.openai.com/
Ortiz-León, G. N., Loinard, L., Dzib, S. A., et al. 2018, ApJL, 869, L33
Pascucci, I., Apai, D., Luhman, K., et al. 2009, ApJ, 696, 143
Pascucci, I., Beck, T. L., Cabrit, S., et al. 2025, NatAs, 9, 81
Pascucci, I., Herczeg, G., Carr, J. S., & Bruderer, S. 2013, ApJ, 779, 178
Perotti, G., Kurtovic, N. T., Henning, T., et al. 2026, ApJ, 997, 281
Pontoppidan, K. M., Salyk, C., Banzatti, A., et al. 2024, ApJ, 963, 158
Pontoppidan, K. M., Salyk, C., Blake, G. A., et al. 2010, ApJ, 720, 887
Richardson, T., Ginsburg, A., Indebetouw, R., & Robitaille, T. P. 2024, ApJ, 961, 188
Rigby, J., Perrin, M., McElwain, M., et al. 2023, PASP, 135, 048001
Robitaille, T. 2017, sedfitter: a Python SED fitting tool - v1.0 release, v1, Zenodo,doi:10.5281/zenodo.235786
Robitaille, T. P. 2017, A&A, 600, A11
Robitaille, T. P., Whitney, B. A., Indebetouw, R., Wood, K., & Denzmore, P. 2006, ApJS, 167, 256
Roccatagliata, V., Ratzka, T., Henning, T., et al. 2011, A&A, 534, A33
Rocha, W. R. M., McClure, M. K., Sturm, J. A., et al. 2025, A&A, 693, A288
Romero-Mirza, C. E., Banzatti, A., Öberg, K. I., et al. 2024, ApJ, 975, 78
Ruiz-Rodriguez, D. A., González-Ruilova, C., Cieza, L. A., et al. 2025, ApJ, 989, 2
Salyk, C. 2022, csalyk/spectools_ir: First release, v1.0.0 , Zenodo, doi:10.5281/zenodo.5818682
Salyk, C. 2025, spectools_ir: Medium/high-resolution IR molecular spectra analysis tools, Astrophysics Source Code Library, ascl:2503.003
Salyk, C., Pontoppidan, K. M., Blake, G. A., Najita, J. R., & Carr, J. S. 2011, ApJ, 731, 130
Schwarz, K. R., Henning, T., Christiaens, V., et al. 2024, ApJ, 962, 8
Schwarz, K. R., Samland, M., Olofsson, G., et al. 2025, ApJ, 980, 148
Sellek, A. D., & van Dishoeck, E. F. 2025, A&A, 701, A239
Shang, H., Krasnopolsky, R., Liu, C.-F., et al. 2023, ApJL, 945, L1
Sturm, J. A., McClure, M. K., Beck, T. L., et al. 2023, A&A, 679, A138
Sturm, J. A., McClure, M. K., Harsono, D., et al. 2024, A&A, 689, A92
Sullivan, T., Wilking, B. A., Greene, T. P., et al. 2019, AJ, 158, 41
Tabone, B., Bettoni, G., van Dishoeck, E. F., et al. 2023, NatAs, 7, 805
Tabone, B., van Dishoeck, E. F., & Black, J. H. 2024, A&A, 691, A11
Tabone, B., van Hemert, M. C., van Dishoeck, E. F., & Black, J. H. 2021, A&A, 650, A192
Temmink, M., Sellek, A. D., Gasman, D., et al. 2025, A&A, 699, A134
Temmink, M., van Dishoeck, E. F., Grant, S. L., et al. 2024, A&A, 686, A117
Trapman, L., Zhang, K., Rosotti, G. P., et al. 2025, ApJ, 989, 5
Tu, Y., Li, Z.-Y., Zhu, Z., Hsu, C.-Y., & Hu, X. 2025, ApJ, 988, 107
Tyagi, H., Manoj, P., Narang, M., et al. 2025, ApJ, 983, 110
van Dishoeck, E. F., Kristensen, L. E., Mottram, J. C., et al. 2021, A&A, 648, A24
van Dishoeck, E. F., Tychoniec, Ł., Rocha, W. R. M., et al. 2025, A&A, 699, A361
van Gelder, M. L., Francis, L., van Dishoeck, E. F., et al. 2024a, A&A, 692, A197
van Gelder, M. L., Ressler, M. E., van Dishoeck, E. F., et al. 2024b, A&A, 682, A78
Vioque, M., Kurtovic, N. T., Trapman, L., et al. 2025, ApJ, 989, 9
Virtanen, P., Gommers, R., Oliphant, T. E., et al. 2020, NatMe, 17, 261
Vlasblom, M., Temmink, M., Sellek, A. D., & van Dishoeck, E. F. 2025, A&A, 703, A52
Wells, M., Pel, J. W., Glasse, A., et al. 2015, PASP, 127, 646
Wright, G. S., Rieke, G. H., Glasse, A., et al. 2023, PASP, 135, 048003
Yang, Y.-L., Green, J. D., Pontoppidan, K. M., et al. 2022, ApJL, 941, L13
Zannese, M., Tabone, B., Habart, E., et al. 2024, NatAs, 8, 577
Zhang, K., Banzatti, A., Salyk, C., et al. 2026, submitted
Zhang, K., Pérez, L. M., Pascucci, I., et al. 2025, ApJ, 989, 1
Zhou, L., Xie, D., & Guo, H. 2015, JChPh, 142, 124317